UC Davis
UC Davis Previously Published Works

Title

Predicting photooxidant concentrations in aerosol liquid water based on laboratory extracts of ambient particles

Permalink

Journal

ISSN

Authors

Ma, Lan
Worland, Reed
Jiang, Wenqing
et al.

Publication Date

DOI

Copyright Information

Peer reviewed

Atmospheric
Chemistry
and Physics

Predicting photooxidant concentrations in aerosol liquid water based on laboratory extracts of ambient particles

Lan Ma[1,a], **Reed Worland**[1,b], **Wenqing Jiang**[2], **Christopher Niedek**[2], **Chrystal Guzman**[1,c], **Keith J. Bein**[3], **Qi Zhang**[2], and **Cort Anastasio**[1]

[1]Department of Land, Air and Water Resources, University of California, Davis,
One Shields Avenue, Davis, CA 95616-8627, USA
[2]Department of Environmental Toxicology, University of California, Davis,
One Shields Avenue, Davis, CA 95616-8627, USA
[3]Center for Health and the Environment, University of California, Davis,
One Shields Avenue, Davis, CA 95616-8627, USA
[a]now at: SGS-CSTC Standards Technical Services Co., Ltd. Hangzhou Branch,
Hangzhou, Zhejiang Province, 310052, China
[b]now at: Department of Chemistry, University of Washington, 1410 Northeast Campus Parkway,
Seattle, WA 98195, USA
[c]now at: Department of Pharmacology, University of Washington, 1410 Northeast Campus Parkway,
Seattle, WA 98195, USA

Correspondence: Cort Anastasio (canastasio@ucdavis.edu)

Abstract. Aerosol liquid water (ALW) is a unique reaction medium, but its chemistry is poorly understood. For example, little is known of photooxidant concentrations – including hydroxyl radicals ($^{\bullet}OH$), singlet molecular oxygen ($^{1}O_2^*$), and oxidizing triplet excited states of organic matter ($^{3}C^*$) – even though they likely drive much of ALW chemistry. Due to the very limited water content of particles, it is difficult to quantify oxidant concentrations in ALW directly. To predict these values, we measured photooxidant concentrations in illuminated aqueous particle extracts as a function of dilution and used the resulting oxidant kinetics to extrapolate to ALW conditions. We prepared dilution series from two sets of particles collected in Davis, California: one from winter (WIN) and one from summer (SUM). Both periods are influenced by biomass burning, with dissolved organic carbon (DOC) in the extracts ranging from 10 to 495 mg C L^{-1}. In the winter sample, the $^{\bullet}OH$ concentration is independent of particle mass concentration, with an average value of $5.0\,(\pm 2.2) \times 10^{-15}$ M, while in summer $^{\bullet}OH$ increases with DOC in the range $(0.4$–$7.7) \times 10^{-15}$ M. In both winter and summer samples, $^{3}C^*$ concentrations increase rapidly with particle mass concentrations in the extracts and then plateau under more concentrated conditions, with a range of $(0.2$–$7) \times 10^{-13}$ M. WIN and SUM have the same range of $^{1}O_2^*$ concentrations, $(0.2$–$8.5) \times 10^{-12}$ M, but in WIN the $^{1}O_2^*$ concentration increases linearly with DOC, while in SUM $^{1}O_2^*$ approaches a plateau.

We next extrapolated the relationships of oxidant formation rates and sinks as a function of particle mass concentration from our dilute extracts to the much more concentrated condition of aerosol liquid water. Predicted $^{\bullet}OH$ concentrations in ALW (including mass transport of $^{\bullet}OH$ from the gas phase) are $(5$–$8) \times 10^{-15}$ M, similar to those in fog/cloud waters. In contrast, predicted concentrations of $^{3}C^*$ and $^{1}O_2^*$ in ALW are approximately 10 to 100 times higher than in cloud/fogs, with values of $(4$–$9) \times 10^{-13}$ M and $(1$–$5) \times 10^{-12}$ M, respectively. Although $^{\bullet}OH$ is often considered the main sink for organic compounds in the atmospheric aqueous phase, the much higher concentrations of $^{3}C^*$ and $^{1}O_2^*$ in aerosol liquid water suggest these photooxidants will be more important sinks for many organics in particle water.

1   Introduction

The chemical processing of organic compounds in cloud/fog water and aerosol liquid water comprises an important source and sink of secondary organic aerosol (SOA) (Carlton et al., 2020; Ervens et al., 2011; Gilardoni et al., 2016; Lim et al., 2010; McNeill, 2015). Aerosol liquid water (ALW), i.e., the liquid-phase water on airborne particles, is much less abundant (in terms of liquid water content) and contains much higher concentrations of solutes compared to clouds and fogs. ALW appears to be an efficient and important medium for the production of aqueous SOA (aqSOA) (Ervens and Volkamer, 2010; Faust et al., 2017; Volkamer et al., 2007; Wu et al., 2018; Zhang et al., 2011), and ALW chemistry is often different from that in more dilute cloud and fog drops (Ervens, 2018; Mekic et al., 2018; Zhou et al., 2019). For example, reactions in ALW can more efficiently produce high-molecular-weight compounds like oligomers and brown carbon (De Haan et al., 2020; Lim et al., 2010; Renard et al., 2014; Tan et al., 2012; Xia et al., 2018). Modeled rates of aqSOA formation in ALW vary enormously, likely because reactant concentrations and chemical processes in particle water are poorly understood (Ervens and Volkamer, 2010; Ervens, 2018; Lin et al., 2014; Washenfelder et al., 2011).

A key driver of ALW reactivity is likely the concentrations of photochemically generated oxidants (Herrmann et al., 2015; Lim et al., 2010). Important aqueous photooxidants include hydroxyl radicals ($^\bullet$OH), oxidizing triplet excited states of organic compounds ($^3C^*$), and singlet molecular oxygen ($^1O_2^*$) (Kaur et al., 2019). $^\bullet$OH is the most widely studied oxidant due to its ubiquity and high reactivity: it reacts with most organics with near-diffusion-controlled rate constants (Herrmann et al., 2015). The main sources of aqueous $^\bullet$OH include mass transfer from the gas phase; the photo-Fenton reaction; and photolysis of nitrate, nitrite, and other species (Anastasio and McGregor, 2001; Arakaki and Faust, 1998; Badali et al., 2015; Herrmann et al., 2010; Tilgner and Herrmann, 2018), while the main sinks of $^\bullet$OH are dissolved organic compounds (Anastasio and Newberg, 2007; Arakaki et al., 2013). Based on lab studies of rainwater, clouds/fogs, and aqueous particle extracts, concentrations of $^\bullet$OH in atmospheric waters (including calculated rates of gas-to-particle partitioning of $^\bullet$OH) are typically 10^{-16}–10^{-15} M (Albinet et al., 2010; Anastasio and McGregor, 2001; Anastasio and Newberg, 2007; Arakaki et al., 2013; Faust and Allen, 1993; Kaur et al., 2019; Leresche et al., 2021; Zhou et al., 2008). In contrast, modeled $^\bullet$OH concentrations in aqueous aerosol are generally 10^{-13} to 10^{-12} M (Ervens et al., 2014; Tilgner and Herrmann, 2018; Tilgner et al., 2013), but these are likely overestimates, in part because of missing $^\bullet$OH sinks (Arakaki et al., 2013; Arciva et al., 2022).

When organic chromophores (i.e., brown carbon) absorb sunlight, the molecules are promoted to their more reactive triplet excited states, some of which are oxidants (Kaur et al., 2019; McNeill and Canonica, 2016). These oxidizing triplets can transform numerous atmospheric species, including converting phenols and biogenic volatile compounds to aqSOA and oxidizing sulfite to sulfate (González Palacios et al., 2016; Monge et al., 2012; Rossignol et al., 2014; Smith et al., 2014; Wang et al., 2020). Triplets can be important oxidants in atmospheric and surface waters, with concentrations of 10^{-15}–10^{-13} M (Kaur and Anastasio, 2018; Kaur et al., 2019; McNeill and Canonica, 2016). In comparison, triplet concentrations in ALW are expected to be higher because the production rate of $^3C^*$ increases with dissolved organic carbon (Canonica and Freiburghaus, 2001; McCabe and Arnold, 2017), although organic compounds can also be important sinks for $^3C^*$, suppressing its steady-state concentration (Gemayel et al., 2021; Wenk et al., 2013). This dual effect of organic compounds makes it difficult to predict $^3C^*$ concentrations in ALW. Kaur et al. (2019) estimated a concentration of oxidizing $^3C^*$ in ALW of 10^{-13}–10^{-11} M based on measurements in dilute particle extracts, while Tilgner et al. (2021) estimated the ALW concentration of triplets as 10^{-11} M.

Most or all of atmospheric triplets (i.e., both oxidizing and non-oxidizing triplets) also transfer energy to dissolved oxygen to form another important photooxidant, singlet molecular oxygen. Concentrations of $^1O_2^*$ in fog/cloud drops and dilute extracts of ambient particles and lab SOA are higher than concentrations of $^\bullet$OH and $^3C^*$, typically 10^{-14} to 10^{-12} M (Anastasio and McGregor, 2001; Bogler et al., 2022; Faust and Allen, 1992; Kaur and Anastasio, 2017; Kaur et al., 2019; Li et al., 2019; Manfrin et al., 2019). Though $^1O_2^*$ is generally less reactive than $^\bullet$OH and $^3C^*$, it can react quickly with certain alkenes, furans, nitrogen heterocycles, polycyclic aromatic hydrocarbons, and other organics (Barrios et al., 2021; Wilkinson et al., 1995) and can be a competitive oxidant because of its high concentration (Bogler et al., 2022; Kaur et al., 2019; Manfrin et al., 2019). Kaur et al. (2019) estimated $^1O_2^*$ might be as high as 10^{-10} M under ALW conditions due to increased $^3C^*$ concentrations, which would make it an important oxidant in particle water (Ma et al., 2021).

Due to its limited water content, it is difficult to study chemistry in ALW directly. To get around this problem, Kaur et al. (2019) measured $^\bullet$OH, $^3C^*$, and $^1O_2^*$ kinetics as a function of dilution in extracts of a single particulate matter (PM) sample and extrapolated the results to aqueous aerosol conditions. However, there are large uncertainties with this extrapolation, since the PM extracts were approximately 1000 times more dilute than ALW conditions. In addition, these authors only examined a single sample collected during winter and were unaware that triplet measurements can be impacted by probe inhibition from organic compounds. To build on this past work, here we apply the same method but with

higher dissolved organic matter concentrations in particle extracts and with correction for triplet probe inhibition. Moreover, in this work we study both a winter PM sample and summer wildfire particles to explore differences in oxidant kinetics.

2 Experimental methods

2.1 Chemicals

Furfuryl alcohol (FFA, 98 %), benzoic acid (BA, ≥ 99.5 %), p-hydroxybenzoic acid (p-HBA, 99 %), (phenylthio)acetic acid (PTA, 96 %), syringol (SYR, 99 %), 3,4-dimethoxybenzaldehyde (DMB, 99 %), and deuterium oxide (99.9 % D atom) were received from MilliporeSigma. All chemical solutions and particulate matter extracts were prepared using air-saturated ultrapure water (Milli-Q water) from a Milli-Q Advantage A10 system (Millipore; $\geq 18.2\,M\Omega\,cm$) with an upstream cartridge to remove organics.

2.2 Particle collection and extraction

Fine particles (PM$_{2.5}$) were collected on the roof of Ghausi Hall on the campus of the University of California, Davis, in February and August 2020. Davis air quality in winter is often impacted by residential wood combustion, while the August 2020 samples were impacted by northern California wildfires. PM$_{2.5}$ was collected using a high-volume sampler equipped with a PM$_{10}$ inlet (Graseby Andersen) to remove PM larger than 10 μm followed by two offset, slotted impactor plates (Tisch Environmental, Inc., 230 series) to remove PM above 2.5 μm. The resulting fine particles were collected onto Teflon-coated borosilicate glass microfiber filters (Pall Corporation, Emfab™ filters, 8 in. × 10 in.) that were pre-cleaned by gently shaking in Milli-Q water for 8 h and then drying at 100 °C. During sampling, the airflow rate was maintained at 68 ($\pm$ 2) m^3 h^{-1}. Particles were collected for either 24 h or up to a week; see Table S1 for details. Upon collection, each sample was wrapped in aluminum foil (baked previously at 500 °C for 8 h), sealed in a Ziploc bag, and frozen at -20 °C. Field blanks were obtained in an identical manner to samples, including loading the clean filters into the sampler and turning on the pump for 2 min.

To prepare particulate matter extracts (PMEs), filters were cut into 2 cm × 2 cm squares on the day of extraction. Each square was placed in an individual, sealed, 20 mL amber glass vial and extracted with Milli-Q water by shaking for 4 h in the dark. The extracts from the same filter sample were combined, filtered (0.22 μm PTFE; Pall), and adjusted to pH 4.2 with sulfuric acid or sodium hydroxide to mimic the acidity of winter particle water in the Central Valley of California (Parworth et al., 2017). The pH of each extract was measured by a pH microelectrode (MI-414 series, protected tip; Microelectrodes, Inc.). The UV–Vis spectrum of each

PME was measured in a 1 cm cuvette immediately after pH adjustment with a Shimadzu UV-2501PC spectrophotometer. Rates of sunlight absorption between 300 and 450 nm were calculated for midday winter-solstice sunlight in Davis, as described by Kaur et al. (2019). PMEs were divided into 4 mL HDPE bottles and flash-frozen in liquid nitrogen immediately after preparation and were later thawed on the day of experiments. Filter squares were weighed by a microbalance (Sartorius M2P) before and after extraction to determine the PM mass extracted; the resulting PM mass / water mass ratios in the filtered extracts might be overestimated because of removal of insoluble material during filtration. Dissolved organic carbon (DOC) and major ion concentrations (Table S2) in PMEs were measured by a Shimadzu TOC-VCPH analyzer and Metrohm ion chromatographs (881 Compact IC Pro) equipped with conductivity detectors, respectively.

To investigate the relationship between particle dilution and oxidant concentration, filter squares from the same sample were extracted with five different volumes of Milli-Q water: 10, 2, 0.7, 0.4, and 0.3 mL. To obtain enough filter squares for this dilution series, for both the winter (WIN) and the summer (SUM) samples we combined extracts from 180 filter squares cut from three sheets of filter that were collected on consecutive days. The same number of squares was cut from each of the three filters in a given sample. We use "PME name-water volume" (e.g., WIN-0.7) to denote the sample and extraction volume. Because it is difficult to extract squares with only 0.4 or 0.3 mL of Milli-Q, for these dilutions we extracted each filter square with 1 mL of Milli-Q and then used a rotary evaporator (Buchi Rotavapor R-110; temperature set no higher than 65 °C) to remove water until we obtained the equivalent of a 0.4 or 0.3 mL extract. We define the concentration factor (CF) of an extract as the inverse of the volume used for extraction. For example, WIN-10 has a concentration factor of 0.1.

2.3 Sample illumination and chemical analysis

We illuminated samples with light from a 1000 W xenon arc lamp passed through a water filter, an AM1.0 air mass filter (AM1D-3L, Sciencetech), and a 295 nm long-pass filter (20CGA-295, Thorlabs) to simulate tropospheric sunlight (Kaur and Anastasio, 2017). We first transferred the extract into a silicone-plugged GE 021 quartz tube (5 mm inner diameter, 1.0 mL volume) and then spiked it with the photooxidant probe and mixed it. The entire tube was illuminated at 20 °C and was not stirred. Dark control samples were wrapped in aluminum foil and kept in the same photoreactor chamber. During illumination, aliquots of approximately 150 μL were removed from the illuminated and dark tubes at specific time intervals to measure concentrations of probes with high-performance liquid chromatography (HPLC, Shimadzu LC-20AB pump, Thermo Scientific Accucore XL C18 column (50 × 3 mm, 4 μm bead), and Shimadzu-M20A UV–Vis detector). The photon flux on each experiment day

was determined by measuring the photolysis rate constant of a 10 μM 2-nitrobenzaldehyde (2NB) solution in the same type of container as samples (Galbavy et al., 2010).

2.4 Photooxidant measurements

Details about determining photooxidant concentrations are provided in past papers (Anastasio and McGregor, 2001; Kaur and Anastasio, 2017; Kaur et al., 2019) and are only discussed briefly here.

2.4.1 Hydroxyl radical (•OH)

The production rate, rate constant for loss, and steady-state concentration of •OH were quantified using benzoic acid (BA) and a competition kinetics technique. A 0.020 M stock solution of benzoic acid / benzoate was prepared and adjusted to pH 4.2. For each sample, four 1.0 mL aliquots of PME were spiked with different final concentrations (100–1200 μM) of BA, keeping PME dilution by the addition of probe solution to less than 10 %. We then illuminated each PME and used HPLC to monitor the formation of p-hydroxybenzoic acid (p-HBA), which is formed from BA oxidation by •OH. The initial rate of p-HBA formation was determined from a regression between concentration and illumination time, using either a linear regression or, for plots with curvature, a three-parameter exponential fit:

$$[p\text{-HBA}]_t = [p\text{-HBA}]_0 + a\left(1 - e^{-bt}\right), \tag{1}$$

where $[p\text{-HBA}]_t$ and $[p\text{-HBA}]_0$ are the concentrations at illumination times t and zero, respectively, and a and b are regression fit parameters. For exponential kinetics data, the initial formation rate of p-HBA, $R_{P,EXP}$, was calculated with

$$R_{P,EXP} = a \times b. \tag{2}$$

Rates of p-HBA formation were normalized to sunlight conditions at midday local time on the winter solstice at Davis (solar zenith angle = 62°; $j_{2NB,win} = 0.0070\,\text{s}^{-1}$; Anastasio and McGregor, 2001), and were corrected for internal light screening due to sample absorption, using

$$R_{P,norm} = \left[\frac{R_{P,EXP}}{S_\lambda \times j_{2NB,EXP}}\right] \times j_{2NB,win}, \tag{3}$$

where S_λ is the internal light screening factor in an individual sample (Table S1) and $j_{2NB,EXP}$ is the photolysis rate constant of 2NB measured on the experiment day.

We then fitted $1/R_{P,norm}$ versus $1/[\text{BA}]$ with a linear regression and used the slope and y intercept to calculate the initial production rate of •OH (P_{OH}), the pseudo-first-order rate constant of •OH loss by natural sinks (k'_{OH}), and the steady-state •OH concentration:

$$P_{OH} = \frac{1}{y \text{ intercept} \times Y_{p\text{-HBA}}}, \tag{4}$$

$$k'_{OH} = k_{BA+\bullet OH}\left(\frac{\text{slope}}{y \text{ intercept}}\right), \tag{5}$$

$$[\bullet OH] = \frac{1}{k_{BA+\bullet OH} \times \text{slope} \times Y_{p\text{-HBA}}}. \tag{6}$$

Here $Y_{p\text{-HBA}}$ (0.18) is the yield of p-HBA from the reaction of BA with •OH (Anastasio and McGregor, 2001) and $k_{BA+\bullet OH}$ is the second-order rate constant of BA reacting with •OH at pH 4.2 ($5.1 \times 10^9\,\text{M}^{-1}\,\text{s}^{-1}$) (Ashton et al., 1995; Wander et al., 1968). •OH measurements are in Table S3.

2.4.2 Oxidizing triplet excited states of organic matter ($^3\text{C}^*$)

Oxidizing triplets were measured employing syringol (SYR) and (phenylthio)acetic acid (PTA) as probes (Kaur and Anastasio, 2018; Ma et al., 2023b). These probes only quantify the subset of triplets that can oxidize organic molecules. SYR captures both weakly and strongly oxidizing triplets, but its decay can be inhibited by dissolved organic matter (DOM) in PME (Canonica and Laubscher, 2008; Ma et al., 2023b; Wenk and Canonica, 2012; Wenk et al., 2015). In contrast, PTA is less sensitive to inhibition by DOM, but it only reacts appreciably with strongly oxidizing triplets (Ma et al., 2023b). Two 1.0 mL aliquots of PME were spiked with 10 μM of SYR or PTA and then illuminated to determine the pseudo-first-order rate constants for the loss of each probe ($k'_{P,EXP}$). Next, $k'_{P,EXP}$ values were normalized to Davis winter sunlight conditions and corrected for light screening using an equation that is analogous to Eq. (3) to obtain rate constant k'_P. The contributions of direct photodegradation, •OH, and $^1\text{O}_2^*$ to probe decay were then subtracted to determine the rate constant for loss of the probe due to triplets, $k'_{P,^3C^*}$:

$$k'_{P,^3C^*} = k'_P - \left(j_P + k_{P+OH}[\bullet OH] + k_{P+1O_2^*}\left[^1\text{O}_2^*\right]\right). \tag{7}$$

Here j_P is the probe direct photodegradation rate constant under Davis winter sunlight, and k_{P+OH} and $k_{P+1O_2^*}$ are the bimolecular rate constants of triplet probes reacting with •OH and $^1\text{O}_2^*$, respectively (Table S4). •OH accounts for 2 %–35 % and 3 %–17 % of the decay of SYR and PTA, respectively, while $^1\text{O}_2^*$ accounts for 3 %–45 % and 2 %–10 % for SYR and PTA (Tables S5 and S6). Since triplets in PMEs represent the excited states of a complex mixture of brown carbon, there is no single value for the second-order rate constant of $^3\text{C}^*$ reacting with probes ($k_{P+^3C^*}$). To estimate triplet concentrations, we assume that triplets ($^3\text{C}^*$) in PME have the same average reactivity as the triplet state of 3,4-dimethoxybenzaldehyde, $^3\text{DMB}^*$ (Fleming et al., 2020; Kaur and Anastasio, 2018; Kaur et al., 2019). Unlike in our

past work (Kaur et al., 2019), we corrected for DOM inhibiting the decays of SYR and PTA, which can cause an underestimate of $^3C^*$ concentrations. To do this, we measured the inhibition factor (IF) in samples (Canonica and Laubscher, 2008; Ma et al., 2023b; Wenk et al., 2011) and used it to correct the $^3C^*$ concentration. Details about inhibition factor measurements and [$^3C^*$] corrections are in Sect. S1 in the Supplement. The $^3C^*$ concentration after inhibition correction is

$$\left[^3C^*\right]_P = \frac{k'_{P,^3C^*}}{k_{P+3DMB^*} \times IF_{P,corr}}, \tag{8}$$

where k_{P+3DMB^*} is the second-order rate constant of the probe with $^3DMB^*$ (Table S4) and $IF_{P,corr}$ is the inhibition factor of the probe in that extract (Table S7). Concentrations of $^3C^*$ in the main text are values after IF correction. While our past work indicates that $^3DMB^*$ is a good surrogate for the average oxidizing triplet in Davis drops and particles (Kaur and Anastasio, 2018; Kaur et al., 2019), it is possible that k_{P+3DMB^*} is higher than the rate constant for the probe with natural triplets. This is the case for surface waters, where the 2,4,6-trimethylphenol (TMP) $+^3DMB^*$ rate constant (Ma et al., 2023b) is 3 times higher than the TMP $+^3CDOM^*$ rate constant (Erickson et al., 2018). If this were also the case for our PM extracts, we would be underestimating oxidizing triplet concentrations by roughly a factor of 3.

2.4.3 Singlet molecular oxygen ($^1O_2^*$)

We used furfuryl alcohol (FFA) as a probe to determine $^1O_2^*$ concentrations (Anastasio and McGregor, 2001; Haag et al., 1984). A total of 1.0 mL of PME sample was divided into two 0.5 mL aliquots, and then one was diluted with 0.5 mL H_2O while the other was diluted with 0.5 mL deuterium oxide (D_2O). A final concentration of 10 µM FFA was spiked into each solution, and then both were illuminated. The pseudo-first-order rate constant of FFA loss in H_2O- and D_2O-diluted PME (k'_{FFA,H_2O} and k'_{FFA,D_2O}) during illumination was determined as the negative slope of a linear regression between $\ln([FFA]_t / [FFA]_0)$ and illumination time (t). The $^1O_2^*$ concentration in the undiluted PME was determined from the difference in FFA loss rates in H_2O and D_2O using (Anastasio and McGregor, 2001)

$$\left[^1O_2^*\right]_{EXP} = \frac{k'_{FFA,D_2O} - k'_{FFA,H_2O}}{D \times k_{FFA+1O_2^*} \times \left(\frac{k'_{H_2O}}{k'_{H_2O}\chi_{H_2O} + k'_{D_2O}\chi_{D_2O}} - 1\right)}, \tag{9}$$

where D is the sample dilution factor (i.e., 0.5 for our experiments); $k_{FFA+1O_2^*}$ is the second-order rate constant of FFA reacting with $^1O_2^*$ at 20 °C, 0.96 (± 0.04) $\times 10^8$ M^{-1} s^{-1} (Appiani et al., 2017); k'_{H_2O} and k'_{D_2O} are the first-order rate constants for loss of $^1O_2^*$ in 100 % H_2O (2.2 $\times 10^5$ s^{-1}) and D_2O (1.6 $\times 10^4$ s^{-1}), respectively (Bilski et al., 1997); and

χ_{H_2O} and χ_{D_2O} are the mole fractions of H_2O and D_2O in the D_2O-diluted solution. Analogously to Eq. (3), we normalized the experimentally determined $^1O_2^*$ concentrations using the light screening factor of each PME and adjustment to Davis winter sunlight conditions. Measurements of $^1O_2^*$ are in Table S8.

3 Results and discussions

3.1 Testing extraction and rotary evaporation

Our winter particle filters were collected in February 2020, when Davis was influenced by residential wood combustion; the average PM$_{2.5}$ concentration during our sampling was 9.2 µg m^{-3}. The summer particles were collected in August 2020, when severe wildfires were occurring approximately 30 km from Davis, resulting in an average PM$_{2.5}$ concentration of 54 µg m^{-3}. While we label our filter composites as "summer" and "winter" as a shorthand, since we have only one sample for each season, our results say little about the seasonality of photooxidants in PM. We explore the issue of oxidant seasonal variations in two other papers (Jiang et al., 2023; Ma et al., 2023a). Figure 1 shows the dissolved organic carbon (DOC) concentrations and rates of light absorption (R_{abs}) as a function of dilution in the winter (WIN) and summer (SUM) particle extracts. We express dilution as the ratio of dry particle mass to liquid water mass in our extracts, since we can experimentally measure these quantities for our PMEs and can estimate values for both clouds/fogs and airborne particles. Both DOC and R_{abs} are directly proportional to the particle mass / water mass ratio, indicating that the extractions of filter squares with varying volumes of water achieved the same extraction efficiency. The DOC values of the most concentrated extracts (−0.4 and −0.3) also follow a linear relationship, showing that the rotary evaporation process used for these dilutions did not lead to significant loss of brown carbon or other organic compounds. As shown in Fig. S1, UV–Vis spectra of the −0.4 and −0.3 extracts before and after rotovapping are essentially the same, indicating that evaporation did not change the brown carbon (BrC) composition significantly. We also checked inorganic concentrations as a function of the concentration factor (Fig. S2): most of the ions exhibit good linearity, indicating consistency in extraction efficiency.

We also examined if rotovapping affects photooxidant concentrations. First, we extracted one filter with either 0.7 mL water per square (sample PME-NR) or 2 mL water per square followed by rotovapping to the equivalent of 0.7 mL water per square (sample PME-R). In a second test, we diluted a rotovapped sample (WIN-0.3) by a factor of 6.7 with water to obtain an extract equivalent to 2 mL Milli-Q per square (WIN-0.3D); this diluted, rotovapped sample should be equivalent to WIN-2, a non-rotovapped sample with the same overall dilution. Figure S3 presents photooxidant concentrations in the two tests. In each test, the concen-
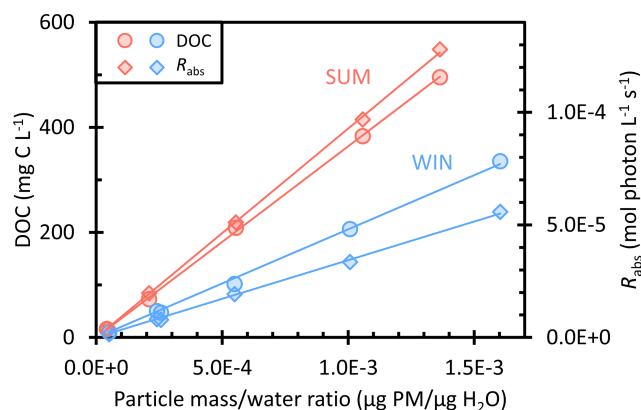
Figure 1. Dependence of dissolved organic carbon (DOC, circles) and the rate of sunlight absorption between 300–450 nm (R_{abs}, diamonds) on the particle mass / water mass ratio (i.e., aqueous particle concentration) in summer (red) and winter (blue) particle extracts.

trations are essentially the same in the rotovapped and non-rotovapped samples, indicating a negligible effect of rotary evaporation on photooxidant kinetics.

3.2   Ions and light absorption

Figure 1 shows that summer and winter PMEs have DOC concentrations in the range of 16–495 and 10–336 mg C L^{-1}, respectively, but WIN has slightly higher particle mass / water mass ratios of $(0.05–1.6) \times 10^{-3}$ µg PM / µg H$_2$O compared to $(0.04–1.4) \times 10^{-3}$ µg PM / µg H$_2$O for SUM. The particle mass / water mass ratios indicate that our extracts have particle concentrations that are equivalent to dilute to concentrated cloud/fog waters. The summer sample of relatively fresh wildfire emissions shows a higher average fraction of organic carbon (OC) to PM mass, 0.37 ($\pm$ 0.02), compared to winter (0.20 ± 0.01). But both are lower than the typical OC / PM ratio near 0.5 for biomass burning particles (Reid et al., 2005; Schauer et al., 2001), probably because our water extracts do not capture non-polar organic compounds. The winter sample has lower organic carbon but higher concentrations of ions, including nitrate (NO$_3^-$), sulfate (SO$_4^{2-}$), and ammonium (NH$_4^+$) (Table S2). For example, nitrate concentrations in WIN range from 0.18 to 5.2 mM and contribute on average ($\pm 1\sigma$) 20 (± 2) % of the total extracted PM mass. In contrast, NO$_3^-$ concentrations in SUM are about 5 times lower (0.03–1.0 mM) at the same concentration factor and only contribute an average of 4.4 (± 0.4) % of the SUM PM mass. The sulfate in WIN accounts for 11 (± 4) % of extracted PM mass, with concentrations (0.03–2.3 mM) that are around 4 times higher than in SUM (0.02–0.6 mM, accounting for an average of 4.2 (± 0.6) % of extracted PM mass). NH$_4^+$ is also higher in WIN (0.20–3.6 mM) compared to SUM (0.10–1.3 mM). Concentrations of potassium, a tracer of biomass burning

(Andreae, 1983), are 0.03–0.7 mM in both WIN and SUM, with a K / PM mass ratio of 0.02 (± 0.004), which is in the range reported for biomass burning aerosols of 0.02 to 0.05 (Reid et al., 2005; Urban et al., 2012).

For all PMEs, absorbance declines exponentially with wavelength (e.g., Fig. S1), and WIN and SUM samples have the same average absorption Ångström exponent (AAE, 300–450 nm) of 7.2 (Table S1), comparable to AAE values (6–8) previously reported in water extracts of biomass burning particles (Hecobian et al., 2010; Hoffer et al., 2006; Kaur et al., 2019). The pathlength-normalized absorption coefficient at 300 nm (α_{300}) for the summer samples (0.2–6.7 cm^{-1}) is about 2 times higher than winter samples at the same concentration factor (0.1–3.0 cm^{-1}) (Table S1). Thus, summer extracts absorb sunlight at approximately twice the rate as winter extracts (Fig. 1). We also calculated the dissolved-organic-carbon-normalized mass absorption coefficient (MAC$_{DOC}$) of each extract by dividing the absorbance at 300 or 365 nm by the DOC concentration (Kaur et al., 2019). SUM average MAC$_{DOC}$ values across all dilutions are 3.1 (± 0.1) and 1.0 (± 0.1) m^2 (g C)$^{-1}$ at 300 and 365 nm, respectively, which are approximately 1.5 times higher than the WIN values (Table S1). This difference is likely because the SUM sample is dominated by fresh wildfire organic aerosols that are composed of organic compounds with a higher degree of unsaturation, increasing light absorption (Fleming et al., 2020). Meanwhile, the WIN sample may contain a lower fraction of fresh biomass burning aerosols due to oxidation and photobleaching of the brown carbon (Forrister et al., 2015; Wong et al., 2019). Our MAC value for WIN is similar to the average MAC value in the previous Davis winter samples (Kaur et al., 2019).

3.3   Photooxidants in PM extracts

In this section we first present our measured oxidant concentrations as a function of particle dilution in the WIN and SUM extracts. We use DOC as the independent variable in our plots because BrC likely dominates the production of ^{3}C* and ^{1}O$_2^*$ and DOC is proportional to the concentration factor in each extract series. We then examine how the production rate (P_{OX}) and pseudo-first-order rate constant for loss (k'_{OX}) for each oxidant vary as a function of dilution. These parameters are related to the oxidant steady-state concentration, [OX], by

$$[OX] = \frac{P_{OX}}{k'_{OX}}. \tag{10}$$

In Sect. 3.4, we extrapolate these kinetic parameters to aerosol liquid water conditions to predict photooxidant concentrations in ALW.

3.3.1 Hydroxyl radicals in PM extracts

As shown in Fig. 2a, the most dilute sample in the WIN dilution series, WIN-10, has the lowest $^\bullet$OH concentration, while in the other dilutions [$^\bullet$OH] is noisy but appears to be independent of DOC. This result, i.e., that $^\bullet$OH concentration is essentially independent of particle mass concentration, is similar to what Kaur et al. (2019) observed for winter samples (green points in Fig. 2), although our $^\bullet$OH concentrations are approximately 10 times higher.

Kaur et al. (2019) found that the $^\bullet$OH photoproduction rate (P_{OH}) and sink (k'_{OH}) both linearly increase with the concentration factor, leading to a roughly constant $^\bullet$OH concentration, since the concentration is equal to the ratio P_{OH}/k'_{OH} (Eq. 10). To explore this in our samples, we determined P_{OH} and k'_{OH} in all of the WIN and SUM extracts; we start by considering the WIN results. As shown in Fig. 3a, P_{OH} and k'_{OH} both increase linearly with DOC, which is consistent with the winter PM extract observations of Kaur et al. (2019), though our samples have a higher slope for P_{OH} and a lower one for k'_{OH}. This higher $^\bullet$OH production rate, coupled with a lower rate constant for $^\bullet$OH loss, is responsible for the roughly 10 times higher [$^\bullet$OH] in this work, but we do not know why these parameters are so different between the previous and current winter particle samples. P_{OH} in WIN ranges from 0.02×10^{-8} to $4.8 \times 10^{-8}\,M\,s^{-1}$, significantly higher than typical values (approximately $10^{-10}\,M\,s^{-1}$) in rainwater, cloud, and fog waters (Albinet et al., 2010; Arakaki et al., 2013; Hong et al., 2018; Kaur and Anastasio, 2018; Tilgner and Herrmann, 2018). In Davis fog samples, the major source of $^\bullet$OH is photolysis of nitrate and nitrite (Anastasio and McGregor, 2001; Kaur and Anastasio, 2017). However, in our winter PM extracts, nitrate accounts for 10 % or less of P_{OH} (Table S3), while the nitrite contribution is negligible. Instead, we hypothesize that our samples might contain higher concentrations of transition metals, contributing to $^\bullet$OH production (Li et al., 2022; Vidrio et al., 2009). While DOC photoreactions can also be a source of $^\bullet$OH (Badali et al., 2015), it seems likely that P_{OH} is correlated with DOC primarily because DOC is a proxy for the concentration factor in the extracts. As for $^\bullet$OH sinks in our WIN extracts, k'_{OH} is in the range $(0.2–9.9) \times 10^6\,s^{-1}$, which is higher than previous Davis fog values $((0.4–1.3) \times 10^6\,s^{-1}$; Kaur and Anastasio, 2017). The lowest k'_{OH} (in WIN-10, the most dilute extract) is comparable to the field blank values (Table S3), suggesting that [$^\bullet$OH] in WIN-10 may be artificially low because of background contamination. We also calculated the rate constant of organics reacting with $^\bullet$OH (k_{DOC+OH}) for the winter samples; our average WIN value, $2.4 (\pm 0.7) \times 10^8\,L\,(mol\,C)^{-1}\,s^{-1}$, is similar to the one determined by Arakaki et al. (2013) for general atmospheric waters, $3.8 (\pm 1.9) \times 10^8\,L\,(mol\,C)^{-1}\,s^{-1}$. In contrast, the average winter k_{DOC+OH} in Kaur et al. (2019) is approximately 3 times higher than our current winter sample; i.e., the past organics were more reactive with $^\bullet$OH.
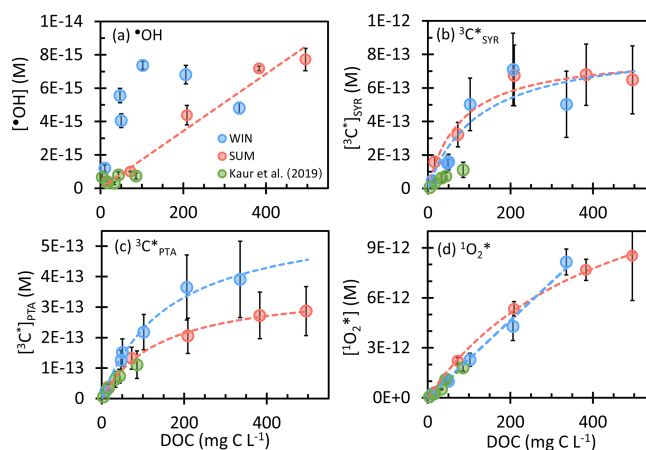

Figure 2. Steady-state concentrations of **(a)** hydroxyl radicals, **(b, c)** oxidizing triplet excited states of brown carbon determined by **(b)** syringol (SYR) and **(c)** (phenylthio)acetic acid (PTA), and **(d)** singlet molecular oxygen in WIN (blue) and SUM (red) samples as a function of dissolved organic carbon. WIN-0.3D results are also included. Previous measurements in Davis winter particle extracts are shown in green (Kaur et al., 2019). Error bars represent ± 1 standard error propagated from linear regression and uncertainties in rate constants. Dashed lines represent linear or hyperbolic regression fits for WIN and SUM samples.

Unlike in WIN, $^\bullet$OH in the summer samples linearly increases with the concentration factor or DOC, with an $^\bullet$OH concentration range of $(0.4–7.7) \times 10^{-15}\,M$ (Fig. 2a). This indicates that either P_{OH} or k'_{OH} does not increase linearly with DOC. As shown in Fig. 3b, k'_{OH} is linear with DOC, but P_{OH} is proportional to the DOC concentration squared. Our interpretation is that $^\bullet$OH production in SUM is a bimolecular reaction rather than a first-order photolysis reaction. The most likely candidate is the photo-Fenton reaction involving soluble reduced iron and hydrogen peroxide (or organic peroxides) (Paulson et al., 2019; Zepp et al., 1992), where the concentrations of both reactants increase with the concentration factor, as does [DOC]. Therefore, although WIN and SUM have roughly similar $^\bullet$OH concentrations, they apparently have different mechanisms governing $^\bullet$OH formation. P_{OH} in SUM is in the range $(0.03–8.2) \times 10^{-8}\,M\,s^{-1}$, with the value in SUM-0.3 nearly double that of WIN-0.3. In contrast, $^\bullet$OH sinks for the summer and winter samples are similar (Fig. 3) and the average k_{DOC+OH} value in SUM is $2.9 (\pm 1.1) \times 10^8\,L\,(mol\,C)^{-1}\,s^{-1}$, not significantly different from the WIN value.

3.3.2 Oxidizing triplet excited states of organic matter in PM extracts

We determined oxidizing triplet concentrations using two probes. Syringol (SYR) is highly reactive towards both strongly and weakly oxidizing triplets, but its decay by $^3C^*$ can be inhibited by antioxidant moieties in DOM, leading
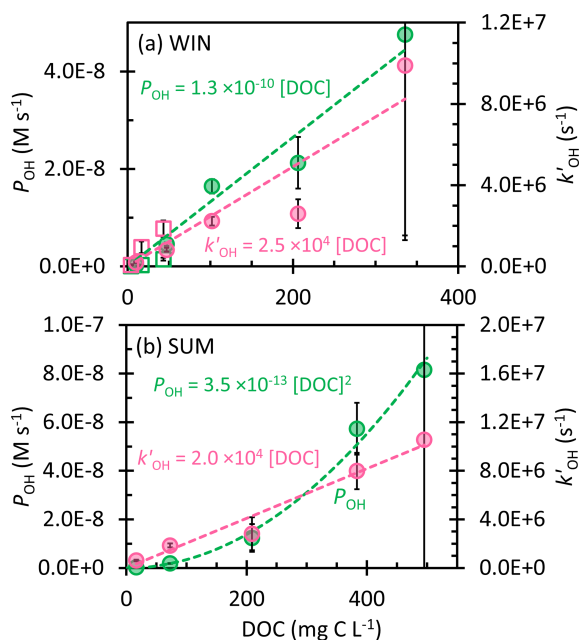
Figure 3. Dependence of the rate of $^\bullet$OH photoproduction (P_{OH}; green, left y axis) and rate constant for loss of $^\bullet$OH due to natural sinks (k'_{OH}; pink, right y axis) on dissolved organic carbon in the **(a)** winter and **(b)** summer samples. Error bars represent ± 1 standard error propagated from the error in regressions and rate constants; error bars for the 0.3 mL extracts (highest DOC) extend past the plot borders. Dashed lines represent linear regression fits, except the dashed green line in **(b)** SUM, which is derived from the linear regression of P_{OH} with $[DOC]^2$. Previous measurements in Davis winter particle extracts are shown as open squares in panel **(a)** (Kaur et al., 2019).

to an underestimate of $^3C^*$ concentrations (Canonica and Laubscher, 2008; Ma et al., 2023b; Maizel and Remucal, 2017; Wenk et al., 2011). (Phenylthio)acetic acid (PTA) has a higher oxidation potential (1.47 V vs. SHE (standard hydrogen electrode), estimated using the Marcus equation) than SYR (~ 1.17 V vs. SHE) (Canonica et al., 2000; Chellamani and Sengu, 2008), is less reactive than SYR with weakly oxidizing triplets, and thus does not capture the whole oxidizing triplet pool. But the advantage of PTA is that it is more resistant to inhibition by DOM (Klein et al., 2006; Ma et al., 2023b). For both probes, we correct for probe inhibition by measuring the inhibition factor (IF) and using it to correct $^3C^*$ concentrations (Sect. S1 and Table S7). Inhibition factors of SYR are as low as 0.13 (± 0.03) in the most concentrated sample (WIN-0.3), indicating that approximately 87 (± 20) % of SYR decay is inhibited by DOM in this sample, which would lead to a $^3C^*$ concentration that is 7.5 (± 1.7) times lower than the actual value if there were no correction for inhibition. This significant inhibition of syringol oxidation is likely due to the high phenolic content of biomass burning particles, whether from residential wood burning (WIN) or wildfires (SUM) (Huo et al., 2021; Schauer

et al., 2001; Wenk and Canonica, 2012), As for PTA, IF values are all greater than 0.9, indicating little inhibition. For simplicity, we only show $^3C^*$ concentrations after inhibition factor correction; uncorrected values are given in Tables S5 and S6.

Concentrations of $^3C^*$ as a function of DOC are in Fig. 2. With SYR as the triplet probe (Fig. 2b), the $[^3C^*]_{SYR}$ range is $(0.5–7.1) \times 10^{-13}$ M in WIN and $(1.6–6.8) \times 10^{-13}$ M in SUM. At the same DOC, $[^3C^*]_{SYR}$ values in summer and winter are similar, despite the differences in sample composition (Table S5). Oxidizing triplet concentrations in our samples are generally higher than those from Kaur et al. (2019) (Fig. 2c, green points), which can be attributed to higher DOC in our samples and our correction for SYR inhibition. From PTA, the $[^3C^*]_{PTA}$ range is $(0.2–3.9) \times 10^{-13}$ M in WIN and $(0.4–2.9) \times 10^{-13}$ M in SUM, with WIN having higher values than SUM at the same concentration factor (Fig. 2c). The $[^3C^*]_{PTA}$ value is lower than $[^3C^*]_{SYR}$ in every dilution, with an average $[^3C^*]_{PTA} / [^3C^*]_{SYR}$ ratio of 0.67 (± 0.22) in WIN and 0.36 (± 0.09) in SUM. Since PTA appears to only capture highly oxidizing triplets (Ma et al., 2022), the ratio of $[^3C^*]_{PTA} / [^3C^*]_{SYR}$ should represent the highly oxidizing fraction of the total oxidizing triplet pool (i.e., 67 % in WIN and 36 % in SUM). Highly oxidizing triplets are typically formed from aromatic ketone or carbonyl precursors, such as 3,4-dimethoxybenzaldehyde, while precursors for weakly oxidizing $^3C^*$ include polycyclic aromatic structures (e.g., 2-acetonaphthone) (McNeill and Canonica, 2016). Our oxidizing triplet concentrations are approximately 100 times higher than $[^\bullet OH]$ (Fig. 2), indicating the likely importance of $^3C^*$ as an oxidant in atmospheric drops and particles.

For both probes, the $^3C^*$ concentration initially increases with DOC but then approaches or reaches a plateau under more concentrated conditions. Kaur et al. (2019) observed the same trend. Their interpretation was that in dilute solutions O_2 is the dominant sink for triplets, while under more concentrated conditions DOM becomes the major sink. Therefore, $^3C^*$ production and loss are both functions of DOC, as described by

$$[^3C^*] = \frac{a[DOC]}{1 + b[DOC]}. \tag{11}$$

The dashed lines in Fig. 2b and c show the regression fitting results of Eq. (11) to the experimental data. From the fitted parameter b (Table S9), we can determine $k_{rxn+Q,3C^*}$ (Eq. S6), the total rate constant of physical quenching and chemical reaction of oxidizing triplets with DOC. Values from our Fig. 2 fittings are $7.6 (\pm 6.8) \times 10^7$ L (mol C)$^{-1}$ s^{-1} for WIN and $1.2 (\pm 0.5) \times 10^8$ L (mol C)$^{-1}$ s^{-1} for SUM (Table S10). Kaur et al. (2019) obtained $9.3 (\pm 1.3) \times 10^7$ L (mol C)$^{-1}$ s^{-1} for Davis winter particle extracts, but they did not correct for SYR inhibition, which should be more significant at higher DOC, leading to an earlier plateau and higher appar-

ent rate constant. Despite this, the three values are not significantly different, possibly because the Kaur et al. (2019) samples had much lower DOC and thus were less affected by SYR inhibition. Wenk et al. (2013) obtained a range of values of $(1.3–3.9) \times 10^7\,\mathrm{L\,(mol\,C)^{-1}\,s^{-1}}$ for surface water DOM quenching and reacting with 2-acetonaphthone and 3-methoxyacetophenone triplets; their lower values imply that atmospheric DOM, at least in our samples, more efficiently quenches triplets than does DOM in surface waters.

The DOC quenching and reaction rate constants from our PTA-derived triplet concentrations are $5.7\,(\pm 1.2) \times 10^7$ and $6.6\,(\pm 1.0) \times 10^7\,\mathrm{L\,(mol\,C)^{-1}\,s^{-1}}$ for WIN and SUM, respectively. These values are lower than those obtained using SYR, as reflected by the weaker curvature of the PTA dashed lines (Fig. 2c) compared to SYR (Fig. 2b). The similar values of $k_{\mathrm{rxn+Q},^3C^*}$ from PTA in WIN and SUM suggest that this rate constant is insensitive to particle type. Therefore, the higher $[^3C^*]_{\mathrm{PTA}}$ in WIN compared to SUM at the same DOC level can be attributed to differences in $^3C^*$ production. This is consistent with the differences in apparent quantum yields: the WIN yield of triplets is 1.8 (± 0.3) %, more than double the SUM value of 0.8 (± 0.1) % (Table S6).

3.3.3 Singlet molecular oxygen in PM extracts

The final photooxidant we measured was singlet molecular oxygen. As shown in Fig. 2d, winter and summer samples have similar $^1O_2^*$ concentrations, in the range of $(0.2–8.5) \times 10^{-12}\,\mathrm{M}$, with values increasing with DOC. The lowest values, in the most dilute extracts, are comparable to fog water concentrations, while our highest concentrations are approximately 4 times higher than those in previous Davis winter particle extracts (Anastasio and McGregor, 2001; Kaur and Anastasio, 2017; Kaur et al., 2019). Singlet oxygen is the most abundant oxidant in our PMEs, with concentrations roughly 10 times higher than $^3C^*$ and 1000 times higher than $^\bullet$OH. In both series of samples, the $^1O_2^*$ concentration increases with DOC, as seen in Kaur et al. (2019). Since brown carbon is the source of $^1O_2^*$, the $^1O_2^*$ production rate increases with DOC. In contrast, the dominant sink for $^1O_2^*$ is water, whose concentration is independent of the sample concentration factor. All three sets of samples in Fig. 2d exhibit very similar relationships between $^1O_2^*$ and DOC, suggesting DOC concentration might be a good predictor of $^1O_2^*$ concentrations in atmospheric waters.

Apparent quantum yields of $^1O_2^*$ are 3.0 (± 0.2) % for WIN and 2.0 (± 0.4) % for SUM (Table S8), which are in the range of typical values for atmospheric waters (Bogler et al., 2022; Kaur and Anastasio, 2017; Kaur et al., 2019; Leresche et al., 2021; Manfrin et al., 2019) and surface waters (Ossola et al., 2021). As described by Ossola et al. (2021), the most accurate determination of quantum yields with simulated sunlight uses a rate of light absorption that accounts for all of the sunlight wavelengths, i.e., out to roughly 700–800 nm. Consistently with our past work (Kaur et al., 2019),

we determined our quantum yields based on sample light absorption from 300–450 nm; as shown in Table S1, rates of light absorption over this range represent 78 (± 3) % of R_{abs} calculated based on the total sunlight absorption. Thus, our $^1O_2^*$ and $^3C^*$ quantum yields would be roughly 29 (± 1) % smaller if calculated using the entire range of solar light absorption.

For WIN, $^1O_2^*$ is linearly related to DOC throughout the dilution series, but in SUM the singlet oxygen concentration exhibits a linear relationship at low DOC and then starts to level off in the more concentrated extracts (Fig. 2d). This curvature has at least two possible explanations. One, as proposed by Kaur et al. (2019), is that $[^1O_2^*]$ stops rising under concentrated solution conditions because organics become the dominant $^1O_2^*$ sink. The second possibility is that under more concentrated conditions, the concentration of $^3C^*$ plateaus, a result of DOC becoming the dominant sink for triplets (e.g., Fig. 2b). Thus, as the solution becomes more concentrated, the production rate of $^1O_2^*$ rises more slowly, causing $[^1O_2^*]$ to start to bend over. In the summer sample of Fig. 2d, the curvature of $^1O_2^*$ is more likely due to this second explanation (i.e., $[^3C^*]$ plateauing) rather than DOC becoming an important $^1O_2^*$ sink because $^1O_2^*$ generally has lower reactivity than triplets with most organics (Arnold, 2014; Canonica et al., 2000; Wilkinson et al., 1995). Based on rough estimates of the composition and reactivity of particulate organics from biomass burning (Kaur et al., 2019), we estimate that DOC accounts for less than 2 % of the $^1O_2^*$ sink in our extracts.

Assuming the leveling-off of $[^3C^*]$ is responsible for the $^1O_2^*$ curvature in the SUM sample, we can derive a kinetic equation for $[^1O_2^*]$ as a function of DOC (Eq. S8), which is analogous to Eq. (11) and is derived in Sect. S2. This equation gives a good fit to the SUM data, as shown by the dashed red line in Fig. 2d. From the parameter b, we calculate that the rate constant for DOC reacting and physically quenching $^1O_2^*$-producing triplet states ($k_{\mathrm{rxn+Q},3C^*}$) is 2.1 $(\pm 0.3) \times 10^7\,\mathrm{L\,(mol\,C)^{-1}\,s^{-1}}$. This is lower than the values acquired from $[^3C^*]_{\mathrm{SYR}}$ and $[^3C^*]_{\mathrm{PTA}}$, which is reasonable since the $^1O_2^*$-derived value represents the whole triplet pool (i.e., all triplets that can undergo energy transfer with dissolved oxygen), which is a larger pool than oxidizing triplets. Our results suggest that the non-oxidizing triplets are less reactive with organics than are oxidizing triplets, leading to a lower rate constant for reaction and quenching by DOC, as seen previously by Canonica et al. (2000).

3.4 Extrapolating photooxidant concentrations to ALW conditions

In the dilution experiments above, we investigated oxidant kinetics and concentrations as a function of the concentration factor, i.e., particle mass / water mass ratio. In this section we extrapolate these relationships from our dilute extract conditions (with PM mass / water mass ratios of (0.04–

$1.6) \times 10^{-3}$ µg PM / µg H_2O) to the much more concentrated conditions of aerosol liquid water (up to ~ 1 µg PM / µg H_2O).

3.4.1 Hydroxyl radicals in ALW

To estimate [•OH] in particle water for WIN, we apply the linear relationships of P_{OH} and k'_{OH} with DOC that we determined in our extracts (Fig. 3a), along with the relationship of [DOC] to the particle mass / water mass ratio, to predict kinetics under more concentrated particle water conditions. Parameters used in the extrapolation are provided in Table S11. Extrapolating to an ALW of 1 µg PM / µg H_2O yields an estimated P_{OH} of 2.7×10^{-5} M s^{-1} and k'_{OH} of 5.0×10^{9} s^{-1}. However, since our aqueous experiments do not include •OH transferred from the gas phase ($P_{OH,gas}$), we added $P_{OH,gas}$ estimated by Kaur et al. (2019) to our extrapolated P_{OH} to calculate $P_{OH,tot}$. We then estimate [•OH] as $P_{OH,tot}$ divided by k'_{OH} (Eq. 10). Estimating [•OH] for the SUM sample is more complicated, since P_{OH} initially increases with DOC squared. We simulate the •OH production rate as a function of DOC by using photo-Fenton reaction rate constants and setting soluble iron and hydrogen peroxide concentrations to fit measured values (Sect. S3). We then apply this simple model to predict P_{OH} for SUM from fog/cloud to ALW conditions. For k'_{OH} in SUM, we use the measured linear dependence on DOC (Fig. 3b).

Figure 4a shows the predicted hydroxyl radical steady-state concentrations for SUM and WIN across a wide range of liquid water content, from dilute cloud/fog drops to concentrated aqueous particle conditions. We also include the winter PM •OH predictions from Kaur et al. (2019) for comparison. For WIN, [•OH] slowly decreases from 1×10^{-14} M in cloud/fog waters (at 3×10^{-5} µg PM / µg H_2O) to 6×10^{-15} M in ALW (at 1 µg PM / µg H_2O). Calculated [•OH] values are higher than measured values, especially under the most dilute conditions, because •OH from gas-phase mass transfer is included in our extrapolation. The •OH trend for WIN is consistent with the result of Kaur et al. (2019), but our concentrations are 6–12 times higher. This is because WIN has a slope of P_{OH} vs. DOC around 4 times higher than that in Kaur et al. (2019), while the slope for k'_{OH} in WIN is slightly lower (Fig. 3a). For our winter sample under dilute conditions, aqueous processes are as important an •OH source as gas-phase transfer (Fig. 4b). However, the aqueous production rate rises more rapidly with PM mass concentration than does gas-phase mass transfer, making aqueous reactions the dominant source of •OH under ALW conditions, where they account for more than 90 % of •OH production. This slower increase in $P_{OH,gas}$ is also responsible for the decreasing [•OH] with increasing PM mass concentration.

For SUM, predicted [•OH] is approximately constant at 4×10^{-15} M under dilute conditions (Fig. 4a), with gas-phase mass transport being the major source of •OH (Fig. 4c). [•OH] then increases to 1×10^{-14} M at

1×10^{-3} µg PM / µg H_2O as the aqueous production rate ($P_{OH,aq}$) increases rapidly and aqueous reactions dominate •OH production. When moving to more concentrated conditions, [•OH] plateaus because we assume the aqueous H_2O_2 concentration reaches a maximum of 100 µM due to equilibrium with the gas phase (Sect. S3). Thereafter, $P_{OH,aq}$ increases linearly, but more slowly, with the PM mass / water mass ratio; since k'_{OH} also increases linearly with the concentration factor, [•OH] remains nearly constant at 9×10^{-15} M for PM / water ratios of roughly 10^{-3} to 1 µg PM / µg H_2O. For both WIN and SUM, our measured •OH concentrations in the most concentrated extracts are approximately an order of magnitude higher than in Kaur et al. (2019), and this difference is maintained throughout the predicted [•OH] to ambient particle water conditions.

3.4.2 Oxidizing triplet concentrations in ALW

To predict $^3C^*$ concentrations in aerosol liquid water, we used the data in Table S11 to extrapolate $^3C^*$ production rates (P_{3C^*}) and sinks (k'_{3C^*}) to concentrated conditions and calculated $^3C^*$ concentrations for syringol (SYR) and (phenylthio)acetic acid (PTA) with Eq. (10). As shown in Fig. 5a and b, measured [$^3C^*$] values in SUM and WIN are higher than the results in Kaur et al. (2019) at the same particle mass / water mass ratio. This is likely due to higher ratios of OC / PM in our samples. In all three sets of samples, [$^3C^*$] rises rapidly with the PM mass / water mass ratio at low DOC and then reaches or approaches a plateau under aqueous aerosol conditions, as the dominant triplet sink transitions from dissolved O_2 to DOC. We believe the production rate of $^3C^*$ linearly increases with particle mass / water mass ratio (P_{3C^*} in Fig. 5c and d), but the sinks for triplets change, as proposed by Kaur et al. (2019). Under dilute conditions, O_2 is a dominant and constant sink (k'_{3C^*,O_2}), causing [$^3C^*$] to increase with an increasing concentration factor. But for our more concentrated extracts (and continuing at higher PM mass / water mass ratios), organic compounds become the major sink for $^3C^*$ (Fig. 5c and d). Thus the ratio of the production rate and sink rate constant becomes constant at higher DOC, causing [$^3C^*$] to plateau. For SYR, we predict WIN and SUM both reach a maximum value of 8×10^{-13} M at 1 µg PM / µg H_2O. This value is 22 times higher than the concentration under the most dilute conditions in WIN and around 8 times higher than the dilute result in SUM. While SUM starts with a higher [$^3C^*$]$_{SYR}$ under dilute conditions, it experiences greater curvature than WIN, apparently because its organic compounds react with and/or physically quench oxidizing triplets more rapidly (i.e., $k'_{3C^*,DOC}$ is larger for SUM than WIN). For both samples, the ALW prediction for [$^3C^*$]$_{SYR}$ is near the geometric mean of the two bounding fits of Kaur et al. (2019). For the lower $^3C^*$ concentrations determined by PTA, SUM and WIN start with essentially the same [$^3C^*$]$_{PTA}$ value, 3×10^{-14} and 2×10^{-14} M, respectively, at
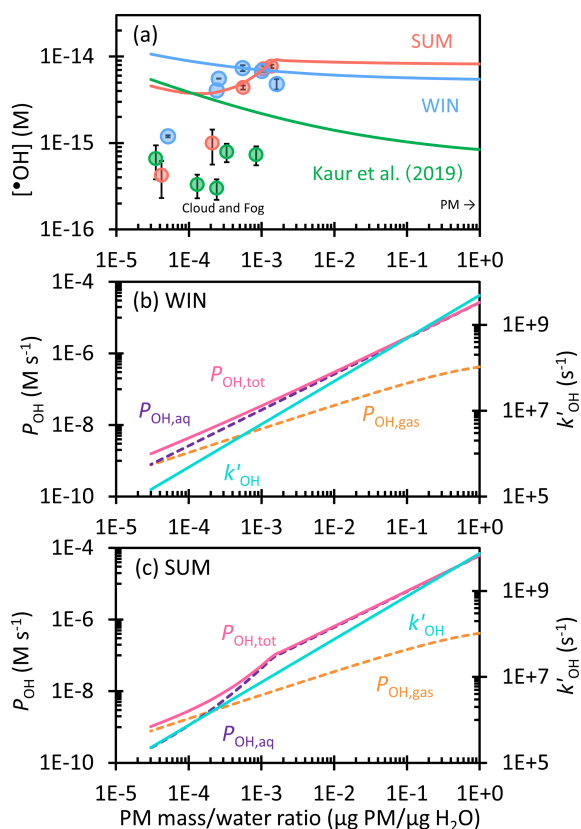
Figure 4. (a) Dependence of hydroxyl radical concentration on the particle mass / water mass ratio in winter (blue) and summer (red) extracts. Solid circles are measured values, while lines are extrapolations to the ambient aqueous aerosol conditions, including contributions from aqueous $^\bullet$OH formation and $^\bullet$OH mass transport from the gas phase. Previous measurements and extrapolation with Davis winter particle extracts are shown in green (Kaur et al., 2019). **(b, c)** Dependence of the hydroxyl radical production rate, including the rate of transport from the gas phase ($P_{OH,gas}$, orange), aqueous reaction ($P_{OH,aq}$, purple), and the total rate ($P_{OH,tot} = P_{OH,aq} + P_{OH,gas}$, pink), and the rate constant of $^\bullet$OH loss by natural sinks (k'_{OH}, blue) on the particle mass / water mass ratio for **(b)** WIN and **(c)** SUM.

3×10^{-5} µg PM / µg H_2O. SUM exhibits more curvature, as seen for $[^3C^*]_{SYR}$, leading to a lower predicted $[^3C^*]_{PTA}$ at 1 µg PM / µg H_2O: 4×10^{-13} M for SUM vs. 6×10^{-13} M for WIN. For SUM and WIN, $[^3C^*]_{PTA}$ increases by factors of 14 and 29, respectively, from the most dilute condition to the ALW condition, which is similar to $[^3C^*]_{SYR}$.

3.4.3 Singlet molecular oxygen in ALW

Lastly, we consider the extrapolation of $^1O_2^*$ concentrations from our dilute experimental solutions to ALW conditions. To do this, we consider the production of $^1O_2^*$ by $^3C^*$ as well as H_2O and DOM as sinks for singlet oxygen. In terms of $^1O_2^*$ sources, we first assume the O_2 concentration is con-

stant at all conditions, i.e., not considering a solute effect on O_2 solubility. Next, we assume the plateauing of $[^3C^*]$ at high concentration factors results in a plateauing of the $^1O_2^*$ production rate, as evidenced in the curvature of $[^1O_2^*]$ in SUM (Fig. 2d). To account for this effect, we fit $[^1O_2^*]$ versus DOC using an equation analogous to Eq. (11) and calculate the $^1O_2^*$ production rate ($P_{1O_2^*}$) with the fitted parameters (Eq. S11). This process does not work for WIN, however, since it shows no curvature of $[^1O_2^*]$. So to predict the $^3C^*$ effect for this sample, we adjusted the regression parameters so that the fitted line passed through just the first four data points (Fig. S6). In terms of modeling DOM as a sink for $^1O_2^*$, this effect does not appear in our lab extracts (due to their relatively low DOC content), but we expect it would happen under more concentrated conditions. To incorporate this effect, we estimated the second-order rate constant for loss of $^1O_2^*$ by DOC ($k_{1O_2^*+DOC}$) using the same approach as in Kaur et al. (2019) but determined a lower value (1×10^5 L (mol C)$^{-1}$ s^{-1}) based on our $^1O_2^*$ concentration data versus DOC. We then calculate the first-order sink for $^1O_2^*$ due to DOC as the product of this second-order rate constant and the DOC concentration.

The resulting predictions for $^1O_2^*$ concentrations, along with the production rate and sink rate constants for the summer sample, are in Fig. 6. Figure 6a shows that our predictions of $^1O_2^*$ under ALW conditions are roughly 10 to 100 times lower than those in Kaur et al. (2019); this is because we include the effect of plateauing $^3C^*$ concentration on the $^1O_2^*$ production rate, which decreases $^1O_2^*$ concentrations under ALW conditions. In Fig. 6a, $[^1O_2^*]$ for SUM starts at 4×10^{-13} M in dilute drops, peaks at 1×10^{-11} M at 1.0×10^{-2} µg PM / µg H_2O (where $P_{1O_2^*}$ first plateaus; Fig. 6b), and then starts to decrease. This decrease is because the production rate for $^1O_2^*$ ($P_{1O_2^*}$) is constant while the $^1O_2^*$ sink from DOC ($k'_{1O_2^*,DOC}$) increases with particle mass concentration and becomes the dominant $^1O_2^*$ sink; the result is a singlet oxygen concentration of 1×10^{-12} M at 1 µg PM / µg H_2O. This concentration is only 1.4 times higher than $[^3C^*]_{SYR}$ under the same conditions (Fig. S8). For WIN, $[^1O_2^*]$ starts at 1×10^{-13} M in dilute drops, reaches a maximum of 3×10^{-11} M at 4.0×10^{-2} µg PM / µg H_2O, and then decreases to 5×10^{-12} M at 1 µg PM / µg H_2O (Fig. S7). Under ALW conditions, WIN has a maximum $[^1O_2^*]$ that is 3 times higher than SUM because measured $[^1O_2^*]$ in WIN presents much less curvature than SUM; i.e., the organics in WIN appear to be less reactive with $^1O_2^*$-producing triplet states compared to those in the SUM sample. Therefore, the plateau of $P_{1O_2^*}$ in WIN shows up only under more concentrated conditions compared to SUM (Fig. S7).
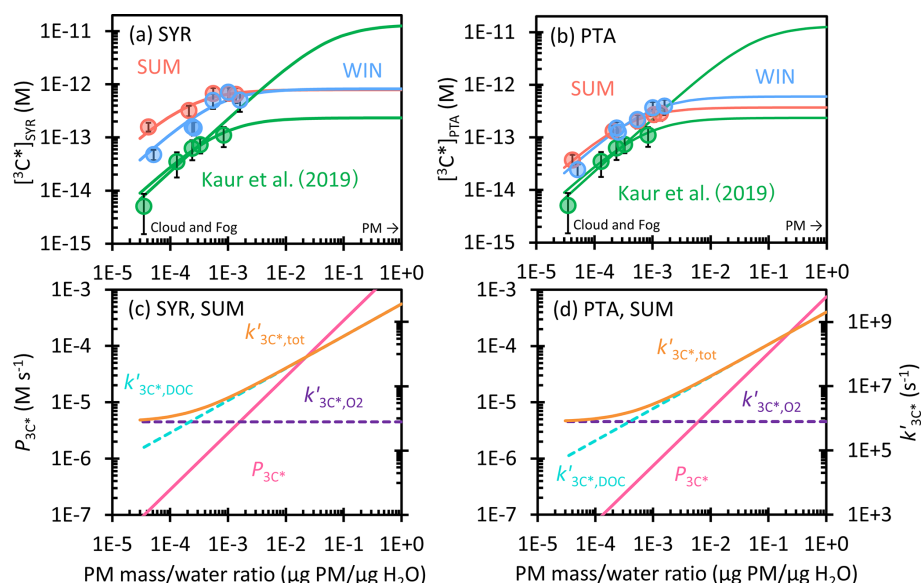
Figure 5. (a, b) Dependence of triplet excited state concentration determined by **(a)** SYR and **(b)** PTA on the particle mass / water mass ratio in WIN (blue) and SUM (red). Solid circles are measured values in dilution experiments, while lines are extrapolations to ALW conditions. Previous measurements and extrapolations (best fit and high estimate) for Davis winter particle extracts are in green (Kaur et al., 2019). **(c, d)** The triplet production rate ($P_{3_{C^*}}$, pink line) and first-order rate constants for $^3C^*$ loss, including quenching by oxygen ($k'_{3_{C^*},O_2}$, dashed purple), dissolved organic carbon ($k'_{3_{C^*},DOC}$, dashed blue), and total ($k'_{3_{C^*},tot} = k'_{3_{C^*},O_2} + k'_{3_{C^*},DOC}$, orange) determined by **(c)** SYR and **(d)** PTA for SUM. Figure S5 shows $P_{3_{C^*}}$ and $k'_{3_{C^*}}$ for WIN.

4 Conclusions and uncertainties

We measured concentrations of three photooxidants – hydroxyl radicals, oxidizing triplet excited states of organic matter, and singlet molecular oxygen – as a function of particle dilution in aqueous extracts of winter particles (influenced by residential wood combustion) and summer particles (strongly influenced by wildfires). The extracts contain high amounts of organic matter, with dissolved organic carbon concentrations ranging from 10 to 495 mg C L^{-1}. DOC-normalized mass absorption coefficients at 300 nm are 2.1 ($\pm$ 0.2) m^2 (g C)$^{-1}$ in winter and 3.1 ($\pm$ 0.1) m^2 (g C)$^{-1}$ in summer, with absorption Ångström exponents of 7.2 for both, indicating significant amounts of brown carbon.

In the winter sample, the measured $^\bullet$OH concentration appears to be independent of extract concentration, while in the summer sample $^\bullet$OH increases with the concentration factor. In both WIN and SUM, measured $^3C^*$ concentrations determined by our two probes initially increase rapidly with the concentration factor and then approach or reach a plateau under more concentrated conditions. Measured $^1O_2^*$ concentrations in WIN are linear with DOC, while in SUM singlet oxygen levels show curvature (like $^3C^*$) in more concentrated extracts. By extrapolating the oxidant kinetics in our dilute extracts to the much more concentrated conditions of ambient particle water (1 µg PM / µg H$_2$O), we obtain photooxidant concentrations of $[^\bullet OH] = (6–9) \times 10^{-15}$ M, $[^3C^*] = (4–8) \times 10^{-13}$ M, and

$[^1O_2^*] = (1–5) \times 10^{-12}$ M. The $^\bullet$OH particle water concentrations are not significantly different from those in fog/cloud waters, while $[^3C^*]$ and $[^1O_2^*]$ are 10–30 and 3–40 times higher, respectively, than fog/cloud values (at 3×10^{-5} µg PM / µg H$_2$O). The ratio of concentrations of $^1O_2^* : {}^3C^* : {}^\bullet OH$ in aerosol liquid water is $10^3–10^2 : 10^2 : 1$, which is lower than the $10^5 : 10^4–10^2 : 1$ ALW ratio predicted by Kaur et al. (2019). This is because our predicted ALW concentration of $^\bullet$OH is approximately 10 times higher than in this past work, while $^3C^*$ is around 5 times higher than their best fit, and $^1O_2^*$ is 30–150 times lower than their prediction (Fig. S8). Kaur et al. (2019) discussed the large uncertainties in predicting $^1O_2^*$ and $^3C^*$ for ALW conditions, in part because of the difficulty in experimentally observing the interactions between DOC and $^3C^*$ or $^1O_2^*$. However, in this current work, we are able to clearly see triplet quenching by DOC, since organic carbon concentrations in our particle water extracts were up to 5 times higher than in the past work. When extrapolating to more concentrated conditions, we predict $^3C^*$ concentrations are heavily suppressed due to quenching by DOC, resulting in triplet concentrations that are between the two estimates from Kaur et al. (2019). For the first time, we also see curvature in $[^1O_2^*]$ versus DOC in our most concentrated summer extracts, which appears to result from suppression of triplets by organics. With this experimental finding, we are able to include this effect in the
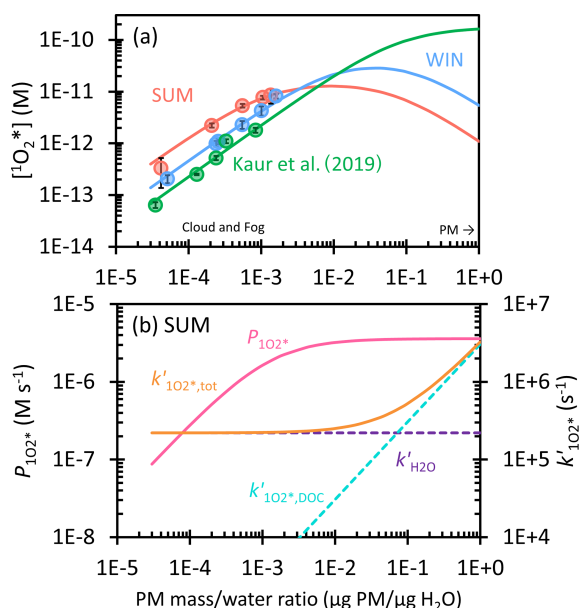
Figure 6. (a) Dependence of singlet molecular oxygen concentration on the particle mass / water mass ratio in winter (blue) and summer (red) samples. Solid circles are measured values in dilution experiments, while lines are extrapolations to ALW conditions. Previous measurements and extrapolation with Davis winter particle extracts are in green (Kaur et al., 2019). **(b)** Dependence of singlet oxygen production rate ($P_{1O_2^*}$, pink line) and the rate constant for $^1O_2^*$ loss, including deactivation by water (k'_{H_2O}, dashed purple), quenching by dissolved organic carbon ($k'_{1O_2^*,DOC}$, dashed blue), and the total sink ($k'_{1O_2^*,tot} = k'_{H_2O} + k'_{1O_2^*,DOC}$, orange) on the particle mass / water mass ratio for SUM. Figure S7 shows $P_{1O_2^*}$ and $k'_{1O_2^*}$ for the winter sample.

prediction of $^1O_2^*$ concentrations under particle water conditions.

While our samples have higher DOC than the dilution sample in Kaur et al. (2019), our extrapolations from dilute extracts to ALW still span a huge range (approximately a factor of 600 in the PM mass / water mass ratio), bringing significant uncertainties. For example, it is unclear whether an appreciable portion of the organic compounds will precipitate under the much more concentrated conditions of ALW. In terms of experimental uncertainties, we could not observe how efficiently organic matter quenches $^1O_2^*$ and thus were only able to estimate an upper bound of the rate constant, which is poorly constrained. In addition, highly concentrated particle extracts make it difficult to measure $^3C^*$ by SYR because of strong inhibition by dissolved organic matter, with inhibition corrections of up to a factor of 7.5 in our samples. Additionally, the difficulty in inhibition factor measurements (and resulting high uncertainties) in concentrated extracts can bring large uncertainties. High DOC concentrations also result in significant light screening, which carries

additional uncertainty in the corresponding correction. While future work could use more concentrated particle extracts to reduce the extrapolation uncertainty, this approach would likely increase other uncertainties, including light screening and probe inhibition. Also, it is unlikely that the bulk solution approach that we have used can ever approach the concentration conditions in particle water. Because of this, other approaches, such as flow tubes or reaction chambers, will be required to more closely simulate oxidant generation and their subsequent reactions in ambient aerosols.

Data availability. All data are available upon request.

Supplement. The supplement related to this article is available online at: https://doi.org/10.5194/acp-23-8805-2023-supplement.

Author contributions. CA and LM developed the research goals and designed the experiments. KJB lent and set up the PM sampler, while LM and CG collected samples. LM and RL performed the photochemistry experiments, while WJ and CN analyzed OC and ions, respectively. LM analyzed the data and prepared the manuscript with contributions from all co-authors. CA reviewed, wrote portions of, and edited the manuscript. CA and QZ provided supervision and oversight during the experiments and writing.

Competing interests. The contact author has declared that none of the authors has any competing interests.

Disclaimer. Publisher's note: Copernicus Publications remains neutral with regard to jurisdictional claims in published maps and institutional affiliations.

Review statement. This paper was edited by Theodora Nah and reviewed by three anonymous referees.

References

Albinet, A., Minero, C., and Vione, D.: Photochemical generation of reactive species upon irradiation of rainwater: negligible photoactivity of dissolved organic matter, Sci. Total Environ., 408, 3367–3373, https://doi.org/10.1016/j.scitotenv.2010.04.011, 2010.

Anastasio, C. and McGregor, K. G.: Chemistry of fog waters in California's Central Valley: 1. In situ photoformation of hydroxyl radical and singlet molecular oxygen, Atmos. Environ., 35, 1079–1089, https://doi.org/10.1016/S1352-2310(00)00281-8, 2001.

Anastasio, C. and Newberg, J. T.: Sources and sinks of hydroxyl radical in sea-salt particles, J. Geophys. Res., 112, D10306, https://doi.org/10.1029/2006JD008061, 2007.

Andreae, M. O.: Soot carbon and excess fine potassium: long-range transport of combustion-derived aerosols, Science, 220, 1148–1151, https://doi.org/10.1126/science.220.4602.1148, 1983.

Appiani, E., Ossola, R., Latch, D. E., Erickson, P. R., and McNeill, K.: Aqueous singlet oxygen reaction kinetics of furfuryl alcohol: effect of temperature, pH, and salt content, Environ. Sci. Process. Impacts, 19, 507–516, https://doi.org/10.1039/C6EM00646A, 2017.

Arakaki, T., Anastasio, C., Kuroki, Y., Nakajima, H., Okada, K., Kotani, Y., Handa, D., Azechi, S., Kimura, T., Tsuhako, A., and Miyagi, Y.: A general scavenging rate constant for reaction of hydroxyl radical with organic carbon in atmospheric waters, Environ. Sci. Technol., 47, 8196–8203, https://doi.org/10.1021/es401927b, 2013.

Arakaki, T. and Faust, B. C.: Sources, sinks, and mechanisms of hydroxyl radical (OH) photoproduction and consumption in authentic acidic continental cloud waters from Whiteface Mountain, New York, The role of the Fe(r) ($r = $ II, III) photochemical cycle, J. Geophys. Res., 103, 3487–3504, https://doi.org/10.1029/97JD02795, 1998.

Arciva, S., Niedek, C., Mavis, C., Yoon, M., Sanchez, M. E., Zhang, Q., and Anastasio, C.: Aqueous •OH oxidation of highly substituted phenols as a source of secondary organic aerosol, Environ. Sci. Technol., 56, 9959–9967, https://doi.org/10.1021/acs.est.2c02225, 2022.

Arnold, W. A.: One electron oxidation potential as a predictor of rate constants of N-containing compounds with carbonate radical and triplet excited state organic matter, Environ. Sci. Process. Impacts, 16, 832–838, https://doi.org/10.1039/c3em00479a, 2014.

Ashton, L., Buxton, G. V., and Stuart, C. R.: Temperature dependence of the rate of reaction of OH with some aromatic compounds in aqueous solution. Evidence for the formation of a ð-complex intermediate?, J. Chem. Soc., 91, 1631–1633, https://doi.org/10.1039/FT9959101631, 1995.

Badali, K. M., Zhou, S., Aljawhary, D., Antiñolo, M., Chen, W. J., Lok, A., Mungall, E., Wong, J. P. S., Zhao, R., and Abbatt, J. P. D.: Formation of hydroxyl radicals from photolysis of secondary organic aerosol material, Atmos. Chem. Phys., 15, 7831–7840, https://doi.org/10.5194/acp-15-7831-2015, 2015.

Barrios, B., Mohrhardt, B., Doskey, P. V., and Minakata, D.: Mechanistic Insight into the Reactivities of Aqueous-Phase Singlet Oxygen with Organic Compounds, Environ. Sci. Technol., 55, 8054–8067, https://doi.org/10.1021/acs.est.1c01712, 2021.

Bilski, P., Holt, R. N., and Chignell, C. F.: Properties of singlet molecular oxygen in binary solvent mixtures of different polarity and proticity, J. Photochem. Photobiol. A, 109, 243–249, https://doi.org/10.1016/S1010-6030(97)00147-0, 1997.

Bogler, S., Daellenbach, K. R., Bell, D. M., Prévôt, A. S. H., El Haddad, I., and Borduas-Dedekind, N.: Singlet oxygen seasonality in aqueous PM_{10} is driven by biomass burning and anthropogenic secondary organic aerosol, Environ. Sci. Technol., 56, 15389–15397, https://doi.org/10.1021/acs.est.2c04554, 2022.

Canonica, S. and Freiburghaus, M.: Electron-rich phenols for probing the photochemical reactivity of freshwaters, Environ. Sci. Technol., 35, 690–695, https://doi.org/10.1021/es0011360, 2001.

Canonica, S., Hellrung, B., and Wirz, J.: Oxidation of phenols by triplet aromatic ketones in aqueous solution, J. Phys. Chem. A, 104, 1226–1232, 2000.

Canonica, S. and Laubscher, H.-U.: Inhibitory effect of dissolved organic matter on triplet-induced oxidation of aquatic contaminants, Photochem. Photobiol. Sci., 7, 547–551, https://doi.org/10.1039/b719982a, 2008.

Carlton, A. G., Christiansen, A. E., Flesch, M. M., Hennigan, C. J., and Sareen, N.: Mulitphase atmospheric chemistry in liquid water: impacts and controllability of organic aerosol, Acc. Chem. Res., 53, 1715–1723, https://doi.org/10.1021/acs.accounts.0c00301, 2020.

Chellamani, A. and Sengu, P.: Mechanistic study on the oxidation of (phenylthio)acetic acids by oxo(salen)manganese(V) complexes and the reactivity–selectivity principle, J. Mol. Catal. A, 283, 83–92, https://doi.org/10.1016/j.molcata.2007.12.004, 2008.

De Haan, D. O., Jansen, K., Rynaski, A. D., Sueme, W. R. P., Torkelson, A. K., Czer, E. T., Kim, A. K., Rafla, M. A., De Haan, A. C., and Tolbert, M. A.: Brown carbon production by aqueous-phase interactions of glyoxal and SO_2, Environ. Sci. Technol., 54, 4781–4789, https://doi.org/10.1021/acs.est.9b07852, 2020.

Erickson, P. R., Moor, K. J., Werner, J. J., Latch, D. E., Arnold, W. A., and McNeill, K.: Singlet Oxygen Phosphorescence as a Probe for Triplet-State Dissolved Organic Matter Reactivity, Environ. Sci. Technol., 52, 9170–9178, https://doi.org/10.1021/acs.est.8b02379, 2018.

Ervens, B.: Progress and problems in modeling chemical processing in cloud droplets and wet aerosol particles, in: Multiphase environmental chemistry in the atmosphere, Vol. 1299, edited by: Hunt, S. W., Laskin, A., and Nizkorodov, S. A., ACS Symposium Series, Vol. 1299, 327–345, American Chemical Society, Washington, DC, ISBN 0841233632, 2018.

Ervens, B. and Volkamer, R.: Glyoxal processing by aerosol multiphase chemistry: towards a kinetic modeling framework of secondary organic aerosol formation in aqueous particles, Atmos. Chem. Phys., 10, 8219–8244, https://doi.org/10.5194/acp-10-8219-2010, 2010.

Ervens, B., Turpin, B. J., and Weber, R. J.: Secondary organic aerosol formation in cloud droplets and aqueous particles (aqSOA): a review of laboratory, field and model studies, Atmos. Chem. Phys., 11, 11069–11102, https://doi.org/10.5194/acp-11-11069-2011, 2011.

Ervens, B., Sorooshian, A., Lim, Y. B., and Turpin, B. J.: Key parameters controlling OH-initiated formation of secondary organic aerosol in the aqueous phase (aqSOA), J. Geophys. Res.-Atmos., 119, 3997–4016, https://doi.org/10.1002/2013JD021021, 2014.

Faust, B. C. and Allen, J. M.: Aqueous-phase photochemical sources of peroxyl radicals and singlet molecular oxygen in clouds and fog, J. Geophys. Res., 97, 12913, https://doi.org/10.1029/92JD00843, 1992.

Faust, B. C. and Allen, J. M.: Aqueous-phase photochemical formation of hydroxyl radical in authentic cloudwa-

ters and fogwaters, Environ. Sci. Technol., 27, 1221–1224, https://doi.org/10.1021/es00043a024, 1993.

Faust, J. A., Wong, J. P. S., Lee, A. K. Y., and Abbatt, J. P. D.: Role of aerosol liquid water in secondary organic aerosol formation from volatile organic compounds, Environ. Sci. Technol., 51, 1405–1413, https://doi.org/10.1021/acs.est.6b04700, 2017.

Fleming, L. T., Lin, P., Roberts, J. M., Selimovic, V., Yokelson, R., Laskin, J., Laskin, A., and Nizkorodov, S. A.: Molecular composition and photochemical lifetimes of brown carbon chromophores in biomass burning organic aerosol, Atmos. Chem. Phys., 20, 1105–1129, https://doi.org/10.5194/acp-20-1105-2020, 2020.

Forrister, H., Liu, J., Scheuer, E., Dibb, J., Ziemba, L., Thornhill, K. L., Anderson, B., Diskin, G., Perring, A. E., Schwarz, J. P., Campuzano-Jost, P., Day, D. A., Palm, B. B., Jimenez, J. L., Nenes, A., and Weber, R. J.: Evolution of brown carbon in wildfire plumes, Geophys. Res. Lett., 42, 4623–4630, https://doi.org/10.1002/2015GL063897, 2015.

Galbavy, E. S., Ram, K., and Anastasio, C.: 2-Nitrobenzaldehyde as a chemical actinometer for solution and ice photochemistry, J. Photochem. Photobiol. A, 209, 186–192, https://doi.org/10.1016/j.jphotochem.2009.11.013, 2010.

Gemayel, R., Emmelin, C., Perrier, S., Tomaz, S., Baboomian, V. J., Fishman, D. A., Nizkorodov, S. A., Dumas, S., and George, C.: Quenching of ketone triplet excited states by atmospheric halides, Environ. Sci.-Atmos., 1, 31–44, https://doi.org/10.1039/D0EA00011F, 2021.

Gilardoni, S., Massoli, P., Paglione, M., Giulianelli, L., Carbone, C., Rinaldi, M., Decesari, S., Sandrini, S., Costabile, F., Gobbi, G. P., Pietrogrande, M. C., Visentin, M., Scotto, F., Fuzzi, S., and Facchini, M. C.: Direct observation of aqueous secondary organic aerosol from biomass-burning emissions, P. Natl. Acad. Sci. USA, 113, 10013–10018, https://doi.org/10.1073/pnas.1602212113, 2016.

González Palacios, L., Corral Arroyo, P., Aregahegn, K. Z., Steimer, S. S., Bartels-Rausch, T., Nozière, B., George, C., Ammann, M., and Volkamer, R.: Heterogeneous photochemistry of imidazole-2-carboxaldehyde: HO_2 radical formation and aerosol growth, Atmos. Chem. Phys., 16, 11823–11836, https://doi.org/10.5194/acp-16-11823-2016, 2016.

Haag, W. R., Hoigné, J., Gassman, E., and Braun, A.: Singlet oxygen in surface waters – Part I: Furfuryl alcohol as a trapping agent, Chemosphere, 13, 631–640, https://doi.org/10.1016/0045-6535(84)90199-1, 1984.

Hecobian, A., Zhang, X., Zheng, M., Frank, N., Edgerton, E. S., and Weber, R. J.: Water-Soluble Organic Aerosol material and the light-absorption characteristics of aqueous extracts measured over the Southeastern United States, Atmos. Chem. Phys., 10, 5965–5977, https://doi.org/10.5194/acp-10-5965-2010, 2010.

Herrmann, H., Hoffmann, D., Schaefer, T., Bräuer, P., and Tilgner, A.: Tropospheric aqueous-phase free-radical chemistry: radical sources, spectra, reaction kinetics and prediction tools, ChemPhysChem, 11, 3796–3822, https://doi.org/10.1002/cphc.201000533, 2010.

Herrmann, H., Schaefer, T., Tilgner, A., Styler, S. A., Weller, C., Teich, M., and Otto, T.: Tropospheric aqueous-phase chemistry: kinetics, mechanisms, and its coupling to a changing gas phase, Chem. Rev., 115, 4259–4334, https://doi.org/10.1021/cr500447k, 2015.

Hoffer, A., Gelencsér, A., Guyon, P., Kiss, G., Schmid, O., Frank, G. P., Artaxo, P., and Andreae, M. O.: Optical properties of humic-like substances (HULIS) in biomass-burning aerosols, Atmos. Chem. Phys., 6 3563–3570, https://doi.org/10.5194/acp-6-3563-2006, 2006.

Hong, J., Liu, J., Wang, L., Kong, S., Tong, C., Qin, J., Chen, L., Sui, Y., and Li, B.: Characterization of reactive photoinduced species in rainwater, Environ. Sci. Pollut. Res. Int., 25, 36368–36380, https://doi.org/10.1007/s11356-018-3499-4, 2018.

Huo, Y., Guo, Z., Li, Q., Wu, D., Ding, X., Liu, A., Huang, D., Qiu, G., Wu, M., Zhao, Z., Sun, H., Song, W., Li, X., Chen, Y., Wu, T., and Chen, J.: Chemical fingerprinting of HULIS in particulate matters emitted from residential coal and biomass combustion, Environ. Sci. Technol., 55, 3593–3603, https://doi.org/10.1021/acs.est.0c08518, 2021.

Jiang, W., Ma, L., Niedek, C., Anastasio, C., and Zhang, Q.: Chemical and Light-Absorption Properties of Water-Soluble Organic Aerosols in Northern California and Photooxidant Production by Brown Carbon Components, ACS Earth Space Chem., 7, 1107–1119, https://doi.org/10.1021/acsearthspacechem.3c00022, 2023.

Kaur, R. and Anastasio, C.: Light absorption and the photoformation of hydroxyl radical and singlet oxygen in fog waters, Atmos. Environ., 164, 387–397, https://doi.org/10.1016/j.atmosenv.2017.06.006, 2017.

Kaur, R. and Anastasio, C.: First measurements of organic triplet excited states in atmospheric waters, Environ. Sci. Technol., 52, 5218–5226, https://doi.org/10.1021/acs.est.7b06699, 2018.

Kaur, R., Labins, J. R., Helbock, S. S., Jiang, W., Bein, K. J., Zhang, Q., and Anastasio, C.: Photooxidants from brown carbon and other chromophores in illuminated particle extracts, Atmos. Chem. Phys., 19, 6579–6594, https://doi.org/10.5194/acp-19-6579-2019, 2019.

Klein, E., Lukeš, V., Cibulková, Z., and Polovková, J.: Study of N–H, O–H, and S–H bond dissociation enthalpies and ionization potentials of substituted anilines, phenols, and thiophenols, J. Mol. Struct.-Theochem., 758, 149–159, https://doi.org/10.1016/j.theochem.2005.10.015, 2006.

Leresche, F., Salazar, J. R., Pfotenhauer, D. J., Hannigan, M. P., Majestic, B. J., and Rosario-Ortiz, F. L.: Photochemical aging of atmospheric particulate matter in the aqueous phase, Environ. Sci. Technol., 55, 13152–13163, https://doi.org/10.1021/acs.est.1c00978, 2021.

Li, J., Chen, Q., Sha, T., and Liu, Y.: Significant promotion of light absorption ability and formation of triplet organics and reactive oxygen species in atmospheric HULIS by fe(iii) ions, Environ. Sci. Technol., 56, 16652–16664, https://doi.org/10.1021/acs.est.2c05137, 2022.

Li, M., Bao, F., Zhang, Y., Sheng, H., Chen, C., and Zhao, J.: Photochemical aging of soot in the aqueous phase: release of dissolved black carbon and the formation of $^1O_2$, Environ. Sci. Technol., 53, 12311–12319, https://doi.org/10.1021/acs.est.9b02773, 2019.

Lim, Y. B., Tan, Y., Perri, M. J., Seitzinger, S. P., and Turpin, B. J.: Aqueous chemistry and its role in secondary organic aerosol (SOA) formation, Atmos. Chem. Phys., 10, 10521–10539, https://doi.org/10.5194/acp-10-10521-2010, 2010.

Lin, G., Sillman, S., Penner, J. E., and Ito, A.: Global modeling of SOA: the use of different mechanisms for

aqueous-phase formation, Atmos. Chem. Phys., 14, 5451–5475, https://doi.org/10.5194/acp-14-5451-2014, 2014.

Ma, L., Guzman, C., Niedek, C., Tran, T., Zhang, Q., and Anastasio, C.: Kinetics and mass yields of aqueous secondary organic aerosol from highly substituted phenols reacting with a triplet excited state, Environ. Sci. Technol., 55, 5772–5781, https://doi.org/10.1021/acs.est.1c00575, 2021.

Ma, L., Worland, R., Heinlein, L., Guzman, C., Jiang, W., Niedek, C., Bein, K. J., Zhang, Q., and Anastasio, C.: Seasonal variations in photooxidant formation and light absorption in aqueous extracts of ambient particles, EGUsphere [preprint], https://doi.org/10.5194/egusphere-2023-861, 2023a.

Ma, L., Worland, R., Tran, T., and Anastasio, C.: Evaluation of probes to measure oxidizing organic triplet excited states in aerosol liquid water, Environ. Sci. Technol., 57, 6052–6062, https://doi.org/10.1021/acs.est.2c09672, 2023b.

Maizel, A. C. and Remucal, C. K.: The effect of probe choice and solution conditions on the apparent photoreactivity of dissolved organic matter, Environ. Sci. Process. Impacts, 19, 1040–1050, https://doi.org/10.1039/c7em00235a, 2017.

Manfrin, A., Nizkorodov, S. A., Malecha, K. T., Getzinger, G. J., McNeill, K., and Borduas-Dedekind, N.: Reactive oxygen species production from secondary organic aerosols: the importance of singlet oxygen, Environ. Sci. Technol., 53, 8553–8562, https://doi.org/10.1021/acs.est.9b01609, 2019.

McCabe, A. J. and Arnold, W. A.: Reactivity of triplet excited states of dissolved natural organic matter in stormflow from mixed-use watersheds, Environ. Sci. Technol., 51, 9718–9728, https://doi.org/10.1021/acs.est.7b01914, 2017.

McNeill, K. and Canonica, S.: Triplet state dissolved organic matter in aquatic photochemistry: reaction mechanisms, substrate scope, and photophysical properties, Environ. Sci. Process. Impacts, 18, 1381–1399, https://doi.org/10.1039/c6em00408c, 2016.

McNeill, V. F.: Aqueous organic chemistry in the atmosphere: sources and chemical processing of organic aerosols, Environ. Sci. Technol., 49, 1237–1244, https://doi.org/10.1021/es5043707, 2015.

Mekic, M., Brigante, M., Vione, D., and Gligorovski, S.: Exploring the ionic strength effects on the photochemical degradation of pyruvic acid in atmospheric deliquescent aerosol particles, Atmos. Environ., 185, 237–242, https://doi.org/10.1016/j.atmosenv.2018.05.016, 2018.

Monge, M. E., Rosenørn, T., Favez, O., Müller, M., Adler, G., Abo Riziq, A., Rudich, Y., Herrmann, H., George, C., and D'Anna, B.: Alternative pathway for atmospheric particles growth, P. Natl. Acad. Sci. USA, 109, 6840–6844, https://doi.org/10.1073/pnas.1120593109, 2012.

Ossola, R., Jönsson, O. M., Moor, K., and McNeill, K.: Singlet oxygen quantum yields in environmental waters, Chem. Rev., 121, 4100–4146, https://doi.org/10.1021/acs.chemrev.0c00781, 2021.

Parworth, C. L., Young, D. E., Kim, H., Zhang, X., Cappa, C. D., Collier, S., and Zhang, Q.: Wintertime water-soluble aerosol composition and particle water content in Fresno, California, J. Geophys. Res.-Atmos., 122, 3155–3170, https://doi.org/10.1002/2016JD026173, 2017.

Paulson, S. E., Gallimore, P. J., Kuang, X. M., Chen, J. R., Kalberer, M., and Gonzalez, D. H.: A light-driven burst of hydroxyl radicals dominates oxidation chemistry in newly activated cloud droplets, Sci. Adv., 5, eaav7689, https://doi.org/10.1126/sciadv.aav7689, 2019.

Reid, J. S., Koppmann, R., Eck, T. F., and Eleuterio, D. P.: A review of biomass burning emissions part II: intensive physical properties of biomass burning particles, Atmos. Chem. Phys., 5, 799–825, https://doi.org/10.5194/acp-5-799-2005, 2005.

Renard, P., Reed Harris, A. E., Rapf, R. J., Ravier, S., Demelas, C., Coulomb, B., Quivet, E., Vaida, V., and Monod, A.: Aqueous phase oligomerization of methyl vinyl ketone by atmospheric radical reactions, J. Phys. Chem. C, 118, 29421–29430, https://doi.org/10.1021/jp5065598, 2014.

Rossignol, S., Aregahegn, K. Z., Tinel, L., Fine, L., Nozière, B., and George, C.: Glyoxal induced atmospheric photosensitized chemistry leading to organic aerosol growth, Environ. Sci. Technol., 48, 3218–3227, https://doi.org/10.1021/es405581g, 2014.

Schauer, J. J., Kleeman, M. J., Cass, G. R., and Simoneit, B. R.: Measurement of emissions from air pollution sources. 3. C_1–C_{29} organic compounds from fireplace combustion of wood, Environ. Sci. Technol., 35, 1716–1728, https://doi.org/10.1021/es001331e, 2001.

Smith, J. D., Sio, V., Yu, L., Zhang, Q., and Anastasio, C.: Secondary organic aerosol production from aqueous reactions of atmospheric phenols with an organic triplet excited state, Environ. Sci. Technol., 48, 1049–1057, https://doi.org/10.1021/es4045715, 2014.

Tan, Y., Lim, Y. B., Altieri, K. E., Seitzinger, S. P., and Turpin, B. J.: Mechanisms leading to oligomers and SOA through aqueous photooxidation: insights from OH radical oxidation of acetic acid and methylglyoxal, Atmos. Chem. Phys., 12, 801–813, https://doi.org/10.5194/acp-12-801-2012, 2012.

Tilgner, A., Bräuer, P., Wolke, R., and Herrmann, H.: Modelling multiphase chemistry in deliquescent aerosols and clouds using CAPRAM3.0i, J. Atmos. Chem., 70, 221–256, https://doi.org/10.1007/s10874-013-9267-4, 2013.

Tilgner, A. and Herrmann, H.: Tropospheric aqueous-phase OH oxidation chemistry: current understanding, uptake of highly oxidized organics and its effects, in: Multiphase environmental chemistry in the atmosphere, Vol. 1299, edited by: Hunt, S. W., Laskin, A., and Nizkorodov, S. A., ACS Symposium Series, Vol. 1299, American Chemical Society, Washington, DC, 49–85, ISBN 0841233632, 2018.

Tilgner, A., Schaefer, T., Alexander, B., Barth, M., Collett Jr., J. L., Fahey, K. M., Nenes, A., Pye, H. O. T., Herrmann, H., and McNeill, V. F.: Acidity and the multiphase chemistry of atmospheric aqueous particles and clouds, Atmos. Chem. Phys., 21, 13483–13536, https://doi.org/10.5194/acp-21-13483-2021, 2021.

Urban, R. C., Lima-Souza, M., Caetano-Silva, L., Queiroz, M. E. C., Nogueira, R. F. P., Allen, A. G., Cardoso, A. A., Held, G., and Campos, M. L. A. M.: Use of levoglucosan, potassium, and water-soluble organic carbon to characterize the origins of biomass-burning aerosols, Atmos. Environ., 61, 562–569, https://doi.org/10.1016/j.atmosenv.2012.07.082, 2012.

Vidrio, E., Phuah, C. H., Dillner, A. M., and Anastasio, C.: Generation of Hydroxyl Radicals from Ambient Fine Particles in a Surrogate Lung Fluid Solution, Environ. Sci. Technol., 43, 922–927, https://doi.org/10.1021/es801653u, 2009.

Volkamer, R., San Martini, F., Molina, L. T., Salcedo, D., Jimenez, J. L., and Molina, M. J.: A missing sink for gas-phase glyoxal in Mexico City: Formation of secondary organic aerosol, Geophys.

Res. Lett., 34, L19807, https://doi.org/10.1029/2007GL030752, 2007.

Wander, R., Neta, P., and Dorfman, L. M.: Pulse radiolysis studies, XII. Kinetics and spectra of the cyclohexadienyl radicals in aqueous benzoic acid solution, J. Phys. Chem., 72, 2946–2949, https://doi.org/10.1021/j100854a044, 1968.

Wang, X., Gemayel, R., Hayeck, N., Perrier, S., Charbonnel, N., Xu, C., Chen, H., Zhu, C., Zhang, L., Wang, L., Nizkorodov, S. A., Wang, X., Wang, Z., Wang, T., Mellouki, A., Riva, M., Chen, J., and George, C.: Atmospheric photosensitization: A new pathway for sulfate formation, Environ. Sci. Technol., 54, 3114–3120, https://doi.org/10.1021/acs.est.9b06347, 2020.

Washenfelder, R. A., Young, C. J., Brown, S. S., Angevine, W. M., Atlas, E. L., Blake, D. R., Bon, D. M., Cubison, M. J., de Gouw, J. A., Dusanter, S., Flynn, J., Gilman, J. B., Graus, M., Griffith, S., Grossberg, N., Hayes, P. L., Jimenez, J. L., Kuster, W. C., Lefer, B. L., Pollack, I. B., Ryerson, T. B., Stark, H., Stevens, P. S., and Trainer, M. K.: The glyoxal budget and its contribution to organic aerosol for Los Angeles, California, during CalNex 2010, J. Geophys. Res., 116, D00V02, https://doi.org/10.1029/2011JD016314, 2011.

Wenk, J., Aeschbacher, M., Sander, M., von Gunten, U., and Canonica, S.: Photosensitizing and inhibitory effects of ozonated dissolved organic matter on triplet-induced contaminant transformation, Environ. Sci. Technol., 49, 8541–8549, https://doi.org/10.1021/acs.est.5b02221, 2015.

Wenk, J. and Canonica, S.: Phenolic antioxidants inhibit the triplet-induced transformation of anilines and sulfonamide antibiotics in aqueous solution, Environ. Sci. Technol., 46, 5455–5462, https://doi.org/10.1021/es300485u, 2012.

Wenk, J., von Gunten, U., and Canonica, S.: Effect of dissolved organic matter on the transformation of contaminants induced by excited triplet states and the hydroxyl radical, Environ. Sci. Technol., 45, 1334–1340, https://doi.org/10.1021/es102212t, 2011.

Wenk, J., Eustis, S. N., McNeill, K., and Canonica, S.: Quenching of excited triplet states by dissolved natural organic matter, Environ. Sci. Technol., 47, 12802–12810, https://doi.org/10.1021/es402668h, 2013.

Wilkinson, F., Helman, W. P., and Ross, A. B.: Rate constants for the decay and reactions of the lowest electronically excited singlet state of molecular oxygen in solution – an expanded and revised compilation, J. Phys. Chem. Ref. Data, 24, 663–677, https://doi.org/10.1063/1.555965, 1995.

Wong, J. P. S., Tsagkaraki, M., Tsiodra, I., Mihalopoulos, N., Violaki, K., Kanakidou, M., Sciare, J., Nenes, A., and Weber, R. J.: Atmospheric evolution of molecular-weight-separated brown carbon from biomass burning, Atmos. Chem. Phys., 19, 7319–7334, https://doi.org/10.5194/acp-19-7319-2019, 2019.

Wu, Z., Wang, Y., Tan, T., Zhu, Y., Li, M., Shang, D., Wang, H., Lu, K., Guo, S., Zeng, L., and Zhang, Y.: Aerosol liquid water driven by anthropogenic inorganic salts: implying its key role in haze formation over the North China Plain, Environ. Sci. Technol. Lett., 5, 160–166, https://doi.org/10.1021/acs.estlett.8b00021, 2018.

Xia, S.-S., Eugene, A. J., and Guzman, M. I.: Cross photoreaction of glyoxylic and pyruvic acids in model aqueous aerosol, J. Phys. Chem. A, 122, 6457–6466, https://doi.org/10.1021/acs.jpca.8b05724, 2018.

Zepp, R. G., Faust, B. C., and Hoigne, J.: Hydroxyl radical formation in aqueous reactions (pH 3–8) of iron(II) with hydrogen peroxide: the photo-Fenton reaction, Environ. Sci. Technol., 26, 313–319, https://doi.org/10.1021/es00026a011, 1992.

Zhang, H., Surratt, J. D., Lin, Y. H., Bapat, J., and Kamens, R. M.: Effect of relative humidity on SOA formation from isoprene/NO photooxidation: enhancement of 2-methylglyceric acid and its corresponding oligoesters under dry conditions, Atmos. Chem. Phys., 11, 6411–6424, https://doi.org/10.5194/acp-11-6411-2011, 2011.

Zhou, W., Mekic, M., Liu, J., Loisel, G., Jin, B., Vione, D., and Gligorovski, S.: Ionic strength effects on the photochemical degradation of acetosyringone in atmospheric deliquescent aerosol particles, Atmos. Environ., 198, 83–88, https://doi.org/10.1016/j.atmosenv.2018.10.047, 2019.

Zhou, X., Davis, A. J., Kieber, D. J., Keene, W. C., Maben, J. R., Maring, H., Dahl, E. E., Izaguirre, M. A., Sander, R., and Smoydzyn, L.: Photochemical production of hydroxyl radical and hydroperoxides in water extracts of nascent marine aerosols produced by bursting bubbles from Sargasso seawater, Geophys. Res. Lett., 35, L20803, https://doi.org/10.1029/2008GL035418, 2008.

Atmospheric
Chemistry
and Physics

Open Access

Supplement of

Predicting photooxidant concentrations in aerosol liquid water based on laboratory extracts of ambient particles

Lan Ma et al.

Correspondence to: Cort Anastasio (canastasio@ucdavis.edu)

Table of contents

Table S1. Particle sample collection and PME information

Sample ID[a]	Collection dates[b]	Sampling duration for each filter[c] (h)	Avg. PM$_{2.5}$ conc.[d] (µg/m^3-air)	Particle mass/water ratio[e] (10^{-4} µg PM/µg H$_2$O)	α_{300}[f] (cm^{-1})	R_{abs} (300-450 nm) (10^{-6} mol-photons L^{-1}s^{-1})[g]	R_{abs} (300-450nm) / R_{abs} (300- λ_{end})[h]	AAE[i]	MAC$_{DOC}$ (m^2 (g C)$^{-1}$)[j] 300 nm	MAC$_{DOC}$ 365 nm	DOC (mg C L^{-1})	Light screening factor[k] PME	Light screening factor PME+ DMB
WIN-10	2/5/20 – 2/28/20	168 (one week)	9.2	0.51 (±0.09)	0.086	1.5	0.84	7.58	2.0	0.57	10.1	0.98	0.75
WIN-2				2.6 (±0.4)	0.446	7.8	0.79	7.28	2.2	0.65	47.2	0.88	N.A.
WIN-0.7				5.5 (±0.9)	1.089	19	0.75	7.23	2.5	0.74	102.1	0.74	0.64
WIN-0.4				10 (±1.5)	1.820	33	0.74	7.02	2.0	0.63	206.3	0.61	N.A.
WIN-0.3				16 (±2.4)	3.029	56	0.74	7.00	2.1	0.65	335.6	0.48	0.40[l]
WIN-0.3D[m]				2.4 (±0.4)	0.452	8.1	0.78	7.16	2.1	0.64	50.2	0.88	0.73
SUM-10	8/21/20 – 8/24/20	28.8	54.5	0.42 (±0.07)	0.220	3.9	0.83	7.42	3.1	0.96	16.4	0.94	0.75
SUM-2				2.1 (±0.4)	1.062	20	0.79	7.17	3.4	1.07	72.7	0.74	N.A.
SUM-0.7				5.5 (±1.3)	2.780	51	0.77	7.17	3.1	0.97	208.9	0.50	0.46
SUM-0.4				11 (±2.3)	5.147	97	0.77	7.05	3.1	0.99	383.4	0.32	N.A.
SUM-0.3				14 (±2.4)	6.679	128	0.74	6.93	3.1	1.01	495.4	0.26	0.23[l]
PME-NR[n]	10/6/20 – 10/8/20	48	30.9	6.4 (±0.2)	1.504	22	0.75	7.57	1.7	0.40	209.9	0.70	0.61
PME-R[n]				6.4 (±0.3)	1.579	23	0.81	7.74	1.8	0.44	204.3	0.68	0.60
Field blanks[o]													
FB1	8/4/20	3 min	6.9	0.16 (±0.06)	0.0022	0.017	1.0				2.1	1	
FB2	1/2/20	3 min	15.6	0.13 (±0.06)	0.0015	0.0013	1.0				2.0	1	
FB3	10/5/20	3 min	39.6	0.47 (±0.38)	0.0065	0.086	1.0				3.0	1	

[a] Samples were named as "PME-water volume" (e.g., WIN-0.7) to denote the sample and extraction volume. WIN-0.3D is the WIN-0.3 sample diluted to an equivalent extract volume of 2 mL/square (i.e., to the equivalent dilution of WIN-2).

[b] For the WIN and SUM samples, we collected three separate, consecutive filters during each collection period and then composited them during extraction. Each winter filter was collected for a week, while each summer filter was collected for approximately 29 hrs. The 10/6/20-10/8/20 sample was just one filter collected for 48 h.

[c] The average sampling duration for each filter within a given composite.

[d] Average PM$_{2.5}$ concentration for each sampling period measured at the UC Davis sampling site by the California Air Resources as reported on the *i*ADAM online database (California Air Resources Board, 2019 −2020; https://www.arb.ca.gov/adam).

[e] Particle mass/water mass ratio (±1 σ) is calculated as the extracted particle mass per filter square (determined as the difference of filter weights before and after extraction) divided by the volume of water used for extraction.

[f] Base-10 absorbance coefficient of the extract (in cm^{-1}) at 300 nm. This is determined as the sample absorbance divided by the cell pathlength.

[g] Rate of sunlight absorption by PME in the 300-450 nm wavelength range, calculated by equation 2 in Kaur et al. (2019), using the actinic flux at midday on the winter solstice in Davis (photons cm^{-2} s^{-1} nm^{-1}) obtained from the Tropospheric Ultraviolet and Visible (TUV) Radiation Model version 4.1. If we apply the actinic flux at midday on the summer solstice, the rate of light absorption is larger by a factor 1.9.

[h] Ratio of the rate of light absorption calculated over a range of 300 to 450 nm to the rate of light absorption calculated from 300 nm to the longest wavelength before the absorbance goes to zero (λ_{end}).

[i] AAE, the Angstrom Absorption Exponent, is calculated as the negative slope of a linear regression between ln(absorbance) vs. ln(wavelength) in the 300 – 450 nm wavelength range.

[j] Mass absorption coefficients at 300 or 365 nm, normalized to dissolved organic carbon, calculated as $MAC_{DOC,300nm} = \frac{\alpha_{300nm,}\times \ln(10)\times 10^6}{[DOC]}$ (Kaur et al., 2019). The contributions of nitrate and nitrite to the total absorbance of PME samples are negligible (< 2 %) for both wavelengths.

[k] Light-absorption-weighted internal screening factor, calculated with equation 2 in Smith et al. (2016) using a wavelength range of 280-364 nm. A value of 1 indicates no light screening, while a low value represents a strong screening effect. "PME" column shows light screening factors in PME samples, while "PME+DMB" column shows values in the PME with added 80 µM DMB (used for inhibition factor measurements; see Section S1). The cell pathlength was 0.5 cm. To save sample volume, *IF* values were not measured for the -2 and -0.4 extracts, so screening factors are not available for these dilutions.

[l] For these very concentrated PME samples, 160 µM DMB was used for inhibition factor measurements. Values shown here are light screening factors of PME with 160 µM DMB.

[m] To test the impact of rotary evaporation on sample composition and photochemistry, this extract was prepared by taking the rotovapped WIN-0.3 extract and diluting it to the same PM mass/water mass ratio as the WIN-2 sample, which was not rotovapped.

[n] To test the impact of rotovapping, this pair of extracts was prepared using portions of the same filter. For the PME-NR sample, the filter was extracted with 0.7 mL water/square and was not rotovapped. For the PME-R sample, the filter was extracted with 2 mL water/square, and was then rotovapped to an equivalent extract volume of 0.7 mL/square.

[o] Field blank samples were extracted with 1.0 mL water/square. Field blank results were not subtracted from sample results.

Table S2. Ion concentrations in PMEs

Sample ID	[NO$_3^-$] (μM)	[NO$_2^-$] (μM)	[SO$_4^{2-}$] (μM)[a]	[Cl$^-$] (μM)	[HCOO$^-$] (μM)	[NH$_4^+$] (μM)	[Na$^+$] (μM)	[K$^+$] (μM)	[Ca^{2+}] (μM)
WIN-10	179.1	< DL[e]	25.0	5.21	2.65	160.8	196.3	34.0	68.8
WIN-2	793.1	3.49	346.9	29.3	30.3	590.4	612.1	98.4	240.3
WIN-0.7	1535	6.49	538.8	20.5	45.9	1826.7	1238.3	261.4	449.9
WIN-0.4	3215	13.6	1435	89.7	116.4	2558.6	2543.9	457.3	149.4
WIN-0.3	5221	21.3	2347	129.2	193.6	3898.2	3601.5	658.4	1214
WIN-0.3D[b]									
SUM-10	27.4	< DL	21.4	5.21	3.53	100.8	134.2	31.5	50.4
SUM-2	137.6	1.95	90.3	23.4	46.0	208.1	276.0	101.1	98.1
SUM-0.7	325.9	2.49	194.1	64.2	92.8	676.4	607.5	315.8	70.5
SUM-0.4	777.7	< DL	478.0	144.7	145.5	1125	1360	561.3	578.6
SUM-0.3	1018	7.85	618.2	184.2	187.9	1330	1717	676.4	696.7
PME-NR	487.0	8.00	352.7	5.21	3.53	1565	1458	356.5	606.6
PME-R	479.7	8.00	349.1	23.4	46.0	1496	1201	517.0	526.7
Field blanks[c]									
FB1[d]	3.12	<DL		2458	3.03	0.12	96.0	-0.02	7.01
FB2	4.58	<DL		1.07	2.94	1.42	93.8	5.92	7.02
FB3	1.99	<DL	12.4	0.65	5.54	1.11	124.6	8.88	7.08

[a] Sulfate from the sulfuric acid added to adjust the sample to pH 4.2 has been subtracted. The added trace-metal grade sulfuric acid contributed an average (± σ) of 40 (± 47) μM sulfate.

[b] Ion concentrations were not measured in this sample.

[c] Field blank results were not subtracted from sample results.

[d] This field blank sample was contaminated by the pH electrode filling solution, resulting in extremely high concentrations of Cl$^-$ and possible other, uncharacterized, contaminants.

[e] Below detection limit.

Table S3. Hydroxyl radical measurements

Sample ID	P_{OH} (10^{-9} M^{-1}s^{-1})[a]	k'_{OH} (10^6 s^{-1})[b]	[•OH] (10^{-15} M)[c]	$10^4 \times \Phi_{OH}$[d]	k_{DOC+OH} (10^8 L (mol-C)$^{-1}$ s^{-1})[e]	%$P_{OH,NO3^-}$[f]
WIN-10	0.24 (± 0.01)	0.20 (± 0.03)	1.2 (± 0.2)	1.7 (± 0.1)	4.5 (± 0.4)	10.4
WIN-2	4.6 (± 0.4)	8.82 (± 0.09)	5.6 (± 0.4)	5.8 (± 0.5)	3.1 (± 0.3)	2.4
WIN-0.7	16.4 (± 1.5)	2.2 (± 0.2)	7.4 (± 0.2)	8.6 (± 0.8)	1.6 (± 0.8)	1.3
WIN-0.4	21.3 (± 5.3)	2.6 (± 0.7)	6.8 (± 0.5)	6.3 (± 1.6)	2.5 (± 0.5)	2.1
WIN-0.3	47.5 (± 41.2)	9.9 (± 8.6)	4.8 (± 0.3)	8.5 (± 7.4)	2.6 (± 3.1)	1.5
WIN-0.3D			4.1 (± 0.4)			
SUM-10	0.26 (± 0.01)	0.61 (± 0.06)	0.43 (± 0.01)	0.67 (± 0.03)	2.4 (± 0.4)	1.5
SUM-2	1.8 (± 0.1)	1.9 (± 0.2)	1.0 (± 0.01)	0.94 (± 0.07)	2.1 (± 0.2)	1.0
SUM-0.7	12.3 (± 5.7)	2.8 (± 1.4)	4.4 (± 0.6)	2.4 (± 1.1)	2.6 (± 0.3)	0.4
SUM-0.4	57.3 (± 10.7)	8.0 (± 1.5)	7.2 (± 0.1)	5.9 (± 1.1)	1.5 (± 0.4)	0.2
SUM-0.3	81.5(± 98.4)	10.6 (± 12.8)	7.7 (± 0.7)	6.4 (± 7.7)	3.5 (± 3.1)	0.2
PME-NR			4.2 (± 0.3)			
PME-R			4.6 (± 0.8)			
Field blanks[g]						
FB1[h]			0.57 (± 0.03)			
FB2[i]	0.0011 (± 0.0001)	0.20 (± 0.02)	0.06 (± 0.01)			5.7
FB3[i]	0.0008 (± 0.0001)	0.05 (± 0.02)	0.15 (± 0.01)			3.6

[a] Davis winter solstice-normalized rate of •OH photoproduction.

[b] Apparent pseudo-first-order rate constant for destruction of •OH due to natural sinks.

[c] Winter solstice-normalized steady-state concentration of •OH.

[d] Apparent quantum yield of •OH during simulated sunlight illumination, calculated as $\Phi_{OH} = P_{OH}/R_{abs}$(300-450).

[e] Second-order rate constant of dissolved organic carbon scavenging •OH, calculated as $k_{DOC+OH} = k'_{OH}$/DOC. The average (± 1σ) values for this rate constant in WIN and SUM dilutions were 2.4 × (±0.7) ×10^8 L (mol-C)$^{-1}$ s^{-1} and 2.9 × (±1.1) ×10^8 L (mol-C)$^{-1}$ s^{-1}, respectively.

[f] Fraction of nitrate contribution to the •OH photoproduction rate, calculated as ($j_{NO3-\rightarrow OH}$ × [NO$_3^-$]/P_{OH}) using the aqueous nitrate photolysis rate constant, $j_{NO3-\rightarrow OH} = 1.4 \times 10^{-7}$ s^{-1} (Anastasio and McGregor, 2001) and the molar concentration of NO$_3^-$. We also calculated the fraction of •OH production rate due to nitrite: it is negligible, with an average value of 1 %.

[g] Field blank results were not subtracted from sample results.

[h] This field blank sample was contaminated by the pH electrode.

[i] The •OH production rate in field blanks was determined by adding 1.2 mM benzoic acid to 1.0 mL FB sample and monitoring the formation of p-hydroxybenzoic acid, assuming that all •OH produced reacts with benzoic acid.

50

55

60

Table S4. Rate constants of SYR and PTA reacting with triplet excited states, singlet oxygen, and hydroxyl radical at pH 4.2

Oxidants	k_{SYR+Ox} (M^{-1} s^{-1})	Reference	k_{PTA+Ox} (M^{-1} s^{-1})	Reference
$^{\bullet}OH$	20 ($\pm$4) $\times$ 10^9	(Smith et al., 2015)	10.3 ($\pm$0.6) $\times$ 10^9	
$^1O_2^*$	3.6 ($\pm$0.7) $\times$ 10^7	(Tratnyek and Hoigne, 1991)	8.8 ($\pm$0.6) $\times$ 10^6	(Ma et al., 2023)
$^3DMB^*$	3.9 ($\pm$0.7) $\times$ 10^9	(Smith et al., 2015)	2.5 ($\pm$0.6) $\times10^9$	
Direct photodegradation	j_{SYR} (s^{-1})		j_{PTA} (s^{-1})	
	$< 4.3 \times 10^{-6}$	(Kaur and Anastasio, 2018)	6.2 ($\pm$0.2) $\times$ 10^{-4}	(Ma et al., 2023)

65

Table S5. Syringol loss kinetics and resulting triplet excited state concentrations

Sample ID	k'_{SYR}[a] $(10^{-2}$ min$^{-1})$	$f_{SYR,OH}$[b]	$f_{SYR,1O2*}$[c]	$f_{SYR,3C*}$[d]	$[^3C^*]_{SYR,uncorr}$[e] $(10^{-14}$ M$)$	$[^3C^*]_{SYR}$[f] $(10^{-14}$ M$)$	$k'_{3C*,SYR}$[g] $(10^6$ s$^{-1})$	$P_{3C*,SYR}$[h] $(10^{-7}$ M s$^{-1})$	$10^2 \times \Phi_{3C*,SYR}$[i]
WIN-10	0.63 (±0.03)	0.23 (±0.06)	0.07 (±0.02)	0.70 (±0.07)	1.9 (±0.4)	4.8 (±1.0)	0.85	0.40 (±0.09)	2.8 (±0.6)
WIN-2	1.9 (±0.1)	0.35 (±0.08)	0.13 (±0.03)	0.52 (±0.09)	4.2 (±1.0)	15 (±4)	1.1	1.6 (±0.5)	2.1 (±0.6)
WIN-0.7	3.7 (±0.2)	0.24 (±0.05)	0.14 (±0.04)	0.62 (±0.09)	9.8 (±2.3)	50 (±16)	1.4	7.2 (±2.4)	3.7 (±1.2)
WIN-0.4	4.6 (±0.2)	0.18 (±0.04)	0.20 (±0.06)	0.62 (±0.08)	12 (±3)	71 (±22)	2.1	15 (±5)	4.4 (±1.3)
WIN-0.3	3.9 (±0.2)	0.15 (±0.03)	0.45 (±0.10)	0.40 (±0.11)	6.7 (±2.3)	50 (±20)	2.9	15 (±6)	2.6 (±1.0)
WIN-0.3D	1.7 (±0.1)	0.28 (±0.06)	0.12 (±0.03)	0.60 (±0.09)	4.5 (±1.0)	16 (±5)	1.1	1.8 (±0.5)	2.2 (±0.6)
SUM-10	2.2 (±0.1)	0.02 (±0.01)	0.03 (±0.01)	0.95 (±0.03)	8.9 (±1.6)	16 (±3)	0.94	1.5 (±0.3)	3.8 (±0.7)
SUM-2	4.5 (±0.1)	0.03 (±0.01)	0.10 (±0.02)	0.87 (±0.03)	17 (±3)	32 (±7)	1.5	4.8 (±1.1)	2.4 (±0.5)
SUM-0.7	8.7 (±0.3)	0.06 (±0.01)	0.13 (±0.03)	0.81 (±0.04)	31 (±6)	68 (±18)	2.8	19 (±5)	3.7 (±1.0)
SUM-0.4	7.9 (±0.1)	0.11 (±0.02)	0.21 (±0.04)	0.68 (±0.05)	23 (±5)	68 (±18)	4.5	31 (±8)	3.2 (±0.9)
SUM-0.3	7.3 (±0.1)	0.13 (±0.03)	0.25 (±0.09)	0.62 (±0.10)	20 (±6)	65 (±20)	5.6	36 (±11)	2.8 (±0.9)
PME-NR	10.7 (±0.3)	0.05 (±0.01)	0.06 (±0.01)	0.89 (±0.03)	41 (±8)	54 (±28)	2.0	11 (±6)	5.0 (±2.6)
PME-R	11.2 (±0.4)	0.05 (±0.01)	0.05 (±0.01)	0.90 (±0.04)	43 (±8)	69 (±15)	2.0	14 (±3)	5.9 (±1.3)
Field blanks[j]									
FB1[k]	0.031 (±0.002)	2.20 (±1.34)	0.11 (±0.02)	-1.31 (±1.34)	-0.018 (±0.018)	-0.32 (±0.33)			
FB2	0.008 (±0.001)	0.09 (±0.02)	0.05 (±0.01)	0.86 (±0.03)	0.30 (±0.05)	0.32 (±0.08)			
FB3	0.12 (±0.01)	0.15 (±0.04)	0.05 (±0.01)	0.80 (±0.06)	0.42 (±0.08)	0.42 (±0.08)			

[a] Davis winter-solstice-normalized pseudo-first-order rate constant for loss of syringol (SYR).

[b] Fraction of SYR loss due to hydroxyl radical, calculated as $f_{SYR,OH} = (k_{SYR+OH} \times [^\bullet OH])/k'_{SYR}$. Hydroxyl radical concentrations are in Table S5.

[c] Fraction of SYR loss due to singlet oxygen, calculated as $f_{SYR,1O2*} = (k_{SYR+1O2*} \times [^1O_2^*])/k'_{SYR}$. Singlet oxygen concentrations are in Table S8.

[d] Fraction of SYR loss due to triplets, calculated as $f_{SYR,3C*} = (1 - f_{SYR,OH} - f_{SYR,1O2*})$.

[e] Uncorrected triplet steady-state concentration calculated from syringol loss as $k'_{SYR,3C*}/k_{SYR+3DMB*}$.

[f] Triplet concentration after correction for inhibition of SYR loss, calculated as $[^3C^*]_{SYR,uncorr}/IF_{SYR,corr}$.

[g] Apparent pseudo-first-order rate constant for quenching of $^3C^*$ due to natural organic sinks and dissolved oxygen, as determined by SYR. This was calculated as $k'_{3C*,SYR} = k_{rxn+Q,3C*}[DOC] + k_{3C*+O2}[O_2]$, where $k_{rxn+Q,3C*}$ is estimated from the fitting between $[^3C^*]_{SYR}$ and DOC using equation (11) in the main text (see values in Table S9), and $k_{3C*+O2} = 2.8 (\pm 0.4) \times 10^9$ M^{-1} s^{-1} from Kaur et al. (2019).

[h] Production rate of triplets determined by SYR, calculated as $P_{3C*,SYR} = [^3C^*]_{SYR} \times k'_{3C*,SYR}$.

[i] Apparent quantum yield of $^3C^*$ determined by SYR during simulated sunlight illumination, calculated as $\Phi_{3C*,SYR} = P_{3C*,SYR}/R_{abs}$.

[j] Field blank results were not subtracted from sample results.

[k] This field blank sample was contaminated by filling solution from a pH electrode.

Table S6. (Phenylthio)acetic acid (PTA) loss kinetics and resulting triplet excited state concentrations

Sample ID	k'_{PTA}[a] (10^{-2} min^{-1})	$f_{PTA,OH}$[b]	$f_{PTA,1O2*}$[c]	$f_{PTA,3C*}$[d]	$[^3C^*]_{PTA,uncorr}$[e] (10^{-14} M)	$[^3C^*]_{PTA}$[f] (10^{-14} M)	$k'_{3C*,PTA}$[g] (10^6 s^{-1})	$P_{3C*,PTA}$[h] (10^{-7} M s^{-1})	$10^2 \times \Phi_{3C*,PTA}$[i]	$[^3C^*]_{PTA}/[^3C^*]_{SYR}$[j]
WIN-10	0.45 (±0.02)	0.17 (±0.03)	0.02 (±0.01)	0.81 (±0.06)	2.4 (±0.06)	2.4 (±0.06)	0.83	0.20 (±0.05)	1.4 (±0.3)	0.51 (±0.17)
WIN-2	2.3 (±0.1)	0.15 (±0.01)	0.03 (±0.01)	0.82 (±0.02)	13 (±3)	13 (±3)	1.0	1.3 (±0.3)	1.6 (±0.4)	0.84 (±0.31)
WIN-0.7	3.8 (±0.1)	0.12 (±0.01)	0.03 (±0.01)	0.85 (±0.04)	22 (±5)	22 (±5)	1.3	2.8 (±0.7)	1.4 (±0.4)	0.43 (±0.18)
WIN-0.4	6.1 (±0.3)	0.07 (±0.01)	0.04 (±0.01)	0.89 (±0.05)	36 (±9)	36 (±9)	1.8	6.4 (±1.6)	1.9 (±0.5)	0.51 (±0.20)
WIN-0.3	6.6 (±0.3)	0.05 (±0.01)	0.06 (±0.01)	0.89 (±0.03)	39 (±10)	39 (±10)	2.4	9.3 (±3.0)	1.8 (±0.5)	0.78 (±0.39)
WIN-0.3D	2.5 (±0.1)	0.10 (±0.01)	0.02 (±0.01)	0.88 (±0.02)	15 (±4)	15 (±4)	1.0	1.6 (±0.5)	1.9 (±0.6)	0.95 (±0.39)
SUM-10	0.57 (±0.02)	0.05 (±0.01)	0.03 (±0.02)	0.92 (±0.04)	0.35 (±0.09)	0.37 (±0.10)	0.87	0.33 (±0.08)	0.85 (±0.21)	0.23 (±0.07)
SUM-2	2.1 (±0.1)	0.03 (±0.01)	0.06 (±0.01)	0.91 (±0.03)	13 (±3)	13 (±4)	1.2	1.6 (±0.4)	0.80 (±0.22)	0.41 (±0.15)
SUM-0.7	3.5 (±0.1)	0.08 (±0.01)	0.08 (±0.01)	0.84 (±0.02)	20 (±5)	21 (±6)	1.9	4.0 (±1.1)	0.78 (±0.22)	0.30 (±0.12)
SUM-0.4	4.9 (±0.1)	0.10 (±0.01)	0.08 (±0.01)	0.82 (±0.03)	27 (±7)	27 (±8)	2.9	7.9 (±2.2)	0.81 (±0.23)	0.40 (±0.16)
SUM-0.3	5.2 (±0.2)	0.09 (±0.01)	0.09 (±0.03)	0.82 (±0.03)	29 (±7)	29 (±8)	3.5	10 (±3)	0.78 (±0.22)	0.44 (±0.19)
PME-NR	4.4 (±0.1)	0.06 (±0.01)	0.03 (±0.01)	0.91 (±0.03)	27 (±7)	28 (±16)	2.1	5.8 (±3.2)	2.6 (±1.5)	0.52 (±0.40)
PME-R	4.8 (±0.1)	0.06 (±0.01)	0.03 (±0.01)	0.91 (±0.02)	29 (±7)	41 (±10)	2.0	8.4 (±2.1)	3.6 (±0.1)	0.60 (±0.20)
Field blanks[k]										
FB1[l]	2.75 (±0.04)	0.01 (±0.01)	0.00 (±0.01)	0.99 (±0.14)	18.1 (±5.0)	20.1 (±7.0)				
FB2	0.016 (±0.005)	0.22 (±0.03)	0.07 (±0.01)	0.71 (±0.32)	0.078 (±0.040)	0.084 (±0.043)				
FB3	0.030 (±0.012)	0.31 (±0.04)	0.05 (±0.01)	0.64 (±0.38)	0.13 (±0.08)	0.13 (±0.08)				

[a] Davis winter-solstice-normalized value of the measured pseudo-first-order rate constant for loss of PTA after correction for PTA direct photodegradation. PTA direct photodegradation accounted for (0.9–12) % of PTA total decay in PME samples, with an average of 3%. It accounted for (2–79) % of PTA total decay in field blanks.

[b] Contribution of hydroxyl radical to the loss of PTA, calculated as $f_{PTA,OH} = (k_{PTA+OH} \times [^{\bullet}OH])/k'_{PTA}$. Hydroxyl radical concentrations are in Table S5.

[c] Contribution of singlet oxygen to the loss of PTA, calculated as $f_{PTA,1O2*} = (k_{PTA+1O2*} \times [^1O_2^*])/k'_{PTA}$. Singlet oxygen concentration is in the Table S8.

[d] Fraction of PTA loss due to triplets, calculated as $f_{PTA,3C*} = (1 - f_{PTA,OH} - f_{PTA,1O2*})$.

[e] Uncorrected triplet steady-state concentration calculated from PTA loss as $k'_{PTA,3C*}/k_{PTA+3DMB*}$.

[f] Triplet concentration after correction for inhibition of PTA loss, calculated as $[^3C^*]_{PTA,uncorr}/IF_{PTA,corr}$.

[g] Apparent pseudo-first-order rate constant for quenching of $^3C^*$ determined by PTA due to natural organic sinks and dissolved oxygen. This was calculated as $k'_{3C*,PTA} = k_{rxn+Q,3C*}[DOC] + k_{3C*+O2}[O_2]$, where $k_{rxn+Q,3C*}$ is estimated from the fitting between $[^3C^*]_{PTA}$ and DOC using equation (10) in the main text (values are in Table S9), and $k_{3C*+O2} = 2.8 (\pm 0.4) \times 10^9$ M^{-1} s^{-1} from Kaur et al. (2019).

[h] Production rate of triplet determined by PTA, calculated as $P_{3C*,PTA} = [^3C^*]_{PTA} \times k'_{3C*,PTA}$.

[i] Apparent quantum yield of $^3C^*$ determined by PTA during simulated sunlight illumination, calculated as $\Phi_{3C*,PTA} = P_{3C*,PTA}/R_{abs}$.

[j] Ratio of triplet concentration determined by PTA to that determined by SYR.

[k] Field blank results were not subtracted from sample results.
[l] This field blank sample was contaminated by a pH electrode, leading to fast decay of PTA.

Section S1. Inhibition factor determination and ^{3}C* concentration correction

Dissolved organic matter in PME may inhibit the decay of SYR or PTA by triplets, leading to an underestimation of triplet concentration. Based on our previous research, SYR is more strongly inhibited than PTA (Ma et al., 2023). To investigate and quantify the inhibition effect of PME on these two triplet

105 probes, we measured inhibition factors (IFs) of FFA, SYR, and PTA for the -10, -0.7 and -0.3 extracts of the WIN and SUM composites, and used the IF values to correct measured ^{3}C* concentrations in PME. Details of inhibition factors are described in Canonica et al. (2008), Wenk et al. (2011), and Ma et al. (2023). To measure IF, we monitored the loss of 10 µM probe in three illuminated solutions: (1) in the pH 4.2 PME; (2) in pH 4.2 Milli-Q water containing 80 µM of triplet precursor 3,4-dimethoxybenzaldehyde

110 (DMB); and (3) in the PME with added DMB (80 µM DMB for the -10 extract and 160 µM DMB for the -0.7 and -0.3 extracts). For each illumination, we determined the first-order rate constant of probe decay. The inhibition factor for the probe in that extract was calculated using

$$IF_P = \frac{k'_{DMB,PME} - k'_{PME}}{k'_{DMB}} \qquad (S1)$$

where $k'_{DMB,PME}$ is the first-order decay rate constant of probe in solution containing both DMB and

115 PME, while k'_{PME} and k'_{DMB} are the probe loss rate constants in PME alone and in Milli-Q water with DMB, respectively. All k' values were corrected for internal light screening with screening factors (S_λ); the PME and PME+DMB values are listed in Table S1, while the light screening factors for 80 and 160 µM DMB are 0.75 and 0.59, respectively. An IF value of 1 indicates there is no DOM inhibition on probe decay, while $IF = 0$ indicates complete inhibition of probe decay. Since IF_P can also be affected by DOM

120 suppressing the ^{3}DMB* concentration, we use IF_{FFA} to quantify this triplet suppression (Ma et al., 2023). To exclude the effect of triplet suppression on IF_{SYR} and IF_{PTA} (i.e., to quantify only inhibition due to probe regeneration), we use corrected inhibition factors, $IF_{SYR,corr}$ and $IF_{PTA,corr}$:

$$IF_{P,corr} = \frac{IF_P}{IF_{FFA}} \qquad (S2)$$

Theoretically, IF should not exceed 1, but we sometimes see this result. When IF_{FFA} or IF_P is greater than

125 1, it suggests there is interaction between DOM in PME with DMB to form reactive species, and thus indicates no inhibition or suppression. Therefore, when IF_{FFA} and/or IF_P is greater than 1, we assume that $IF_{P,corr} = IF_P$, but we do not correct the ^{3}C* concentration if $IF_{P,corr} \geq 1$; i.e., in this latter case $[^3C*]_P = [^3C*]_{P,uncorr}$. More details are provided in Ma et al. (2023). IF_{PTA} and IF_{SYR} values are expected to be lower than IF_{FFA} because IF_{PTA} and IF_{SYR} are affected by both triplet suppression by DOC and probe inhibition

130 by DOC, while IF_{FFA} is only impacted by triplet suppression. However, in some samples IF_{PTA} was

greater than IF_{FFA}; we suspect this might be due to the sometimes large errors in IF_{FFA} measurement, i.e., when the difference between $k'_{DMB,PME}$ and k'_{PME} is small. In this case, we assume $IF_{FFA} = IF_{PTA}$ (since PTA is very resistant to suppression) and use this value to calculate $IF_{P,corr}$. The determined IF and $IF_{P,corr}$ values are shown in Table S4. Due to limited PME volumes, we did not measure IF values for the -2 and -

135   0.4 extracts. Instead, their $IF_{SYR,corr}$ and $IF_{PTA,corr}$ values were estimated from the linear regression of $1/IF_{P,corr}$ from the -10, -0.7, and -0.3 extracts versus DOC (Ma et al., 2023; Wenk et al., 2011).

The uncorrected $^3C^*$ concentration is calculated with:

$$[^3C^*]_{P,uncorr} = \frac{k'_{P,3C*}}{k_{P+3DMB*}}$$ (S3)

where $k'_{P,3C*}$ is the measured first-order rate constant of probe loss due to triplets and $k_{P+3DMB*}$ is the

140   second-order rate constant of probe reacting with $^3DMB^*$. This assumes that the DMB triplet is a reasonable proxy for triplets in atmospheric particles and drops in Davis, as we have shown previously (Kaur and Anastasio, 2018; Kaur et al., 2019). To correct for the probe inhibition effect, $[^3C^*]$ is calculated using

$$[^3C^*]_P = \frac{[^3C^*]_{P,uncorr}}{IF_{P,corr}}$$ (S4)

145   The $^3C^*$ concentrations shown in the main text are the values after IF correction.

Table S7. Inhibition factors for FFA, SYR, and PTA

Sample ID	IF_{FFA}	IF_{SYR}	IF_{PTA}	$IF_{SYR,corr}$	$IF_{PTA,corr}$
WIN-10	0.91 (±0.06)	0.40 (±0.02)	1.00 (±0.04)	0.41 (±0.03)	1.00 (±0.06)
WIN-2[a]				0.28 (±0.04)	1.00 (±0.09)
WIN-0.7	0.62 (±0.10)	0.18 (±0.03)	0.90 (±0.07)	0.20 (±0.04)	1.00 (±0.11)
WIN-0.4[a]				0.17 (±0.04)	1.00 (±0.16)
WIN-0.3	0.28 (±0.08)	0.09 (±0.01)	0.67 (±0.10)	0.13 (±0.03)	1.00 (±0.21)
WIN-0.3D[b]	0.89 (±0.13)	0.25 (±0.02)	0.85 (±0.06)	0.28 (±0.05)	0.97 (±0.17)
SUM-10	1.08 (±0.09)	0.56 (±0.02)	0.95 (±0.08)	0.56 (±0.02)	0.94 (±0.07)
SUM-2[a]				0.53 (±0.07)	0.95 (±0.12)
SUM-0.7	0.48 (±0.06)	0.22 (±0.03)	0.46 (±0.04)	0.45 (±0.09)	0.96 (±0.14)
SUM-0.4[a]				0.35 (±0.06)	0.98 (±0.14)
SUM-0.3	0.19 (±0.12)	0.10 (±0.02)	0.32 (±0.03)	0.30 (±0.06)	1.00 (±0.14)
PME-NR[c]	0.68 (±0.32)	0.52 (±0.05)	0.65 (±0.04)	0.77 (±0.37)	0.95 (±0.48)
PME-R[c]	1.29 (±0.22)	0.63 (±0.07)	0.71 (±0.05)	0.63 (±0.07)	0.71 (±0.05)
Field blanks[d]					
FB1	0.95 (±0.12)	0.52 (±0.05)	0.86 (±0.13)	0.54 (±0.08)	0.90 (±0.19)
FB2	1.10 (±0.05)	0.95 (±0.19)	0.93 (±0.06)	0.95 (±0.19)	0.93 (±0.06)
FB3	1.21 (±0.06)	1.20 (±0.08)	1.15 (±0.09)	1.20 (±0.08)	1.15 (±0.09)

[a] *IF* values in these samples were not measured. $IF_{SYR,corr}$ and $IF_{PTA,corr}$ for these samples were estimated from the linear regressions of $1/IF_{P,corr}$ vs. DOC in each dilution series.

[b] The *IF* values were measured for WIN-0.3D, which had an equivalent dilution to the WIN-2 sample.

[c] IF_{FFA} values for PME-NR and PME-R have large uncertainties because there were very small differences between $k'_{PME,DMB}$ and k'_{PME} for a given extract. In this case a small difference in $k'_{PME,DMB}$ can lead to significant change of IF_{FFA}, likely explaining the very different values of IF_{FFA} in PME-R and PME-NR.

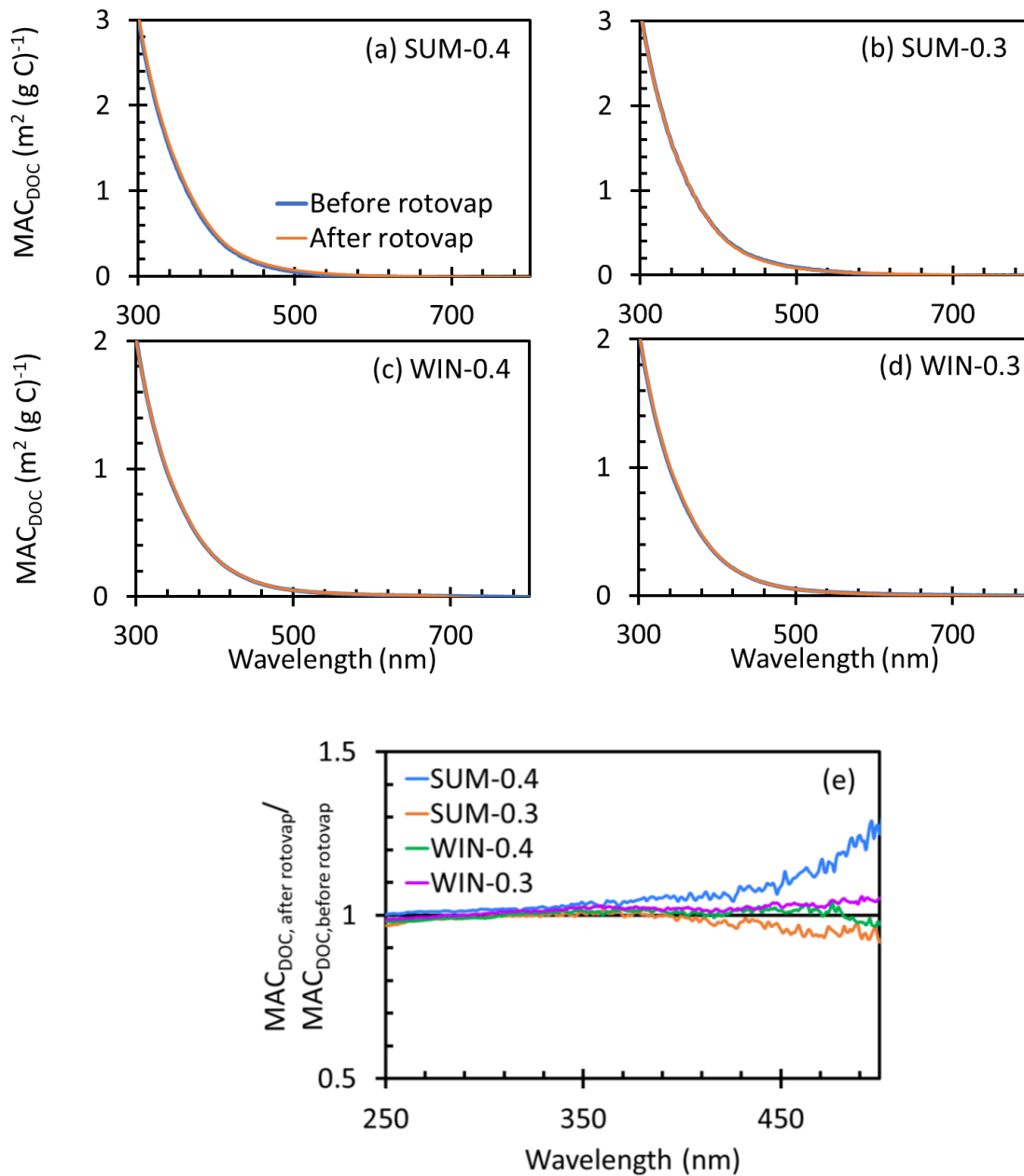[d] Field blank results were not subtracted from sample results.

Figure S1. Mass absorption coefficients in particle extracts normalized by dissolved organic carbon before (blue) and after (orange) rotary evaporation for (a) SUM-0.4, (b) SUM-0.3, (c) WIN-0.4, and (d) WIN-0.3. (e) The ratio of MAC_{DOC} after and before rotary evaporation for the four extracts.
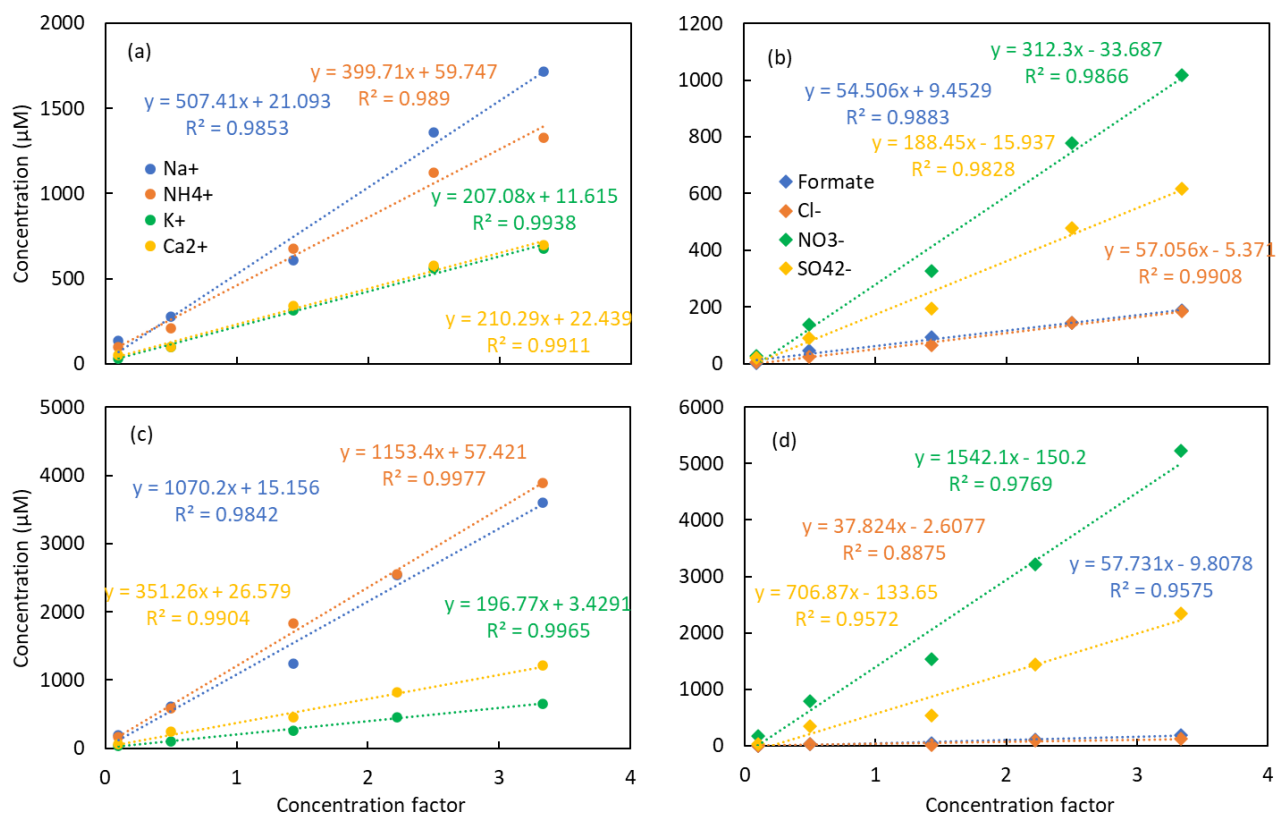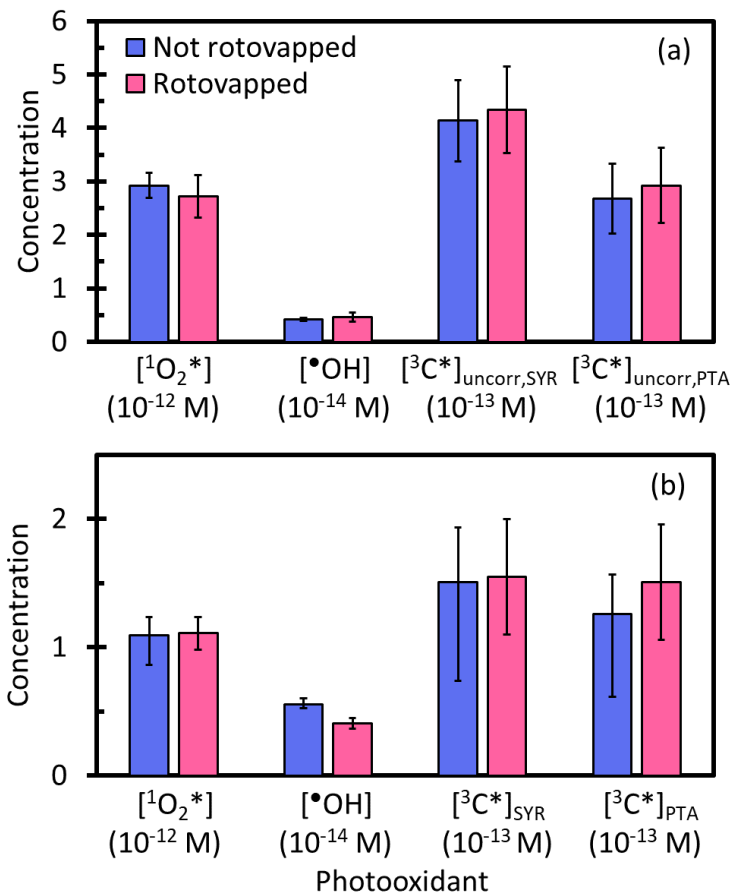
Figure S2. Dependence of concentrations of cations (panel a for SUM and panel c for WIN) and anions (panel b for SUM and panel d for WIN) in particle extracts on concentration factor.

Figure S3. Influence of roto-vapping on steady-state concentrations of $^1O_2^*$, $^\bullet OH$, and $^3C^*$ in not rotovapped (blue) and rotovapped (red) particle extracts of (a) PME-NR vs. PME-R and (b) WIN-2 vs. WIN-0.3D. In each case, the rotovapped sample was concentrated to the concentration factor (i.e., PM mass/water mass ratio) of the not rotovapped sample. Error bars represents ±1 standard error propagated from uncertainties in the kinetic regression and rate constants. In (a) we show $^3C^*$ concentrations that are not *IF*-corrected because IF_{FFA} values for PME-NR and PME-R differ by a factor of nearly two but have large uncertainties (Table S7).

Table S8. Singlet oxygen measurements

Sample ID	$[^1O_2^*]^a$ $(10^{-12}$ M$)$	$P_{1O2*}{}^b$ $(10^{-7}$ M s$^{-1})$	$f_{FFA,1O2*}{}^c$	$f_{FFA,OH}{}^d$	$10^2 \times \Phi_{1O2*}{}^e$	$\Phi_{3C*,SYR}/$ $(\Phi_{1O2*}/f_\Delta)^f$	$\Phi_{3C*,PTA}/$ $(\Phi_{1O2*}/f_\Delta)^g$	$[^3C^*]_{SYR}/[^1O_2^*]^h$	$[^3C^*]_{PTA}/[^1O_2^*]^i$
WIN-10	0.21 (±0.04)	0.45 (±0.08)	0.53 (±0.10)	0.87 (±0.14)	3.1 (±0.5)	0.47 (±0.13)	0.24 (±0.07)	0.23 (±0.07)	0.12 (±0.04)
WIN-2	1.1 (±0.1)	2.4 (±0.3)	0.62 (±0.09)	0.45 (±0.03)	3.1 (±0.4)	0.36 (±0.11)	0.28 (±0.08)	0.14 (±0.04)	0.12 (±0.03)
WIN-0.7	2.3 (±0.4)	5.0 (±0.9)	0.65 (±0.12)	0.61 (±0.02)	2.6 (±0.4)	0.76 (±0.27)	0.29 (±0.09)	0.22 (±0.08)	0.10 (±0.03)
WIN-0.4	4.3 (±0.8)	9.4 (±1.9)	0.69 (±0.14)	0.31 (±0.03)	2.8 (±0.5)	0.84 (±0.30)	0.36 (±0.11)	0.17 (±0.06)	0.09 (±0.03)
WIN-0.3	8.2 (±0.8)	18 (±2)	0.83 (±0.09)	0.14 (±0.01)	3.2 (±0.3)	0.43 (±0.17)	0.27 (±0.09)	0.06 (±0.02)	0.05 (±0.02)
WIN-0.3D	0.98 (±0.13)	2.2 (±0.3)	0.62 (±0.08)	0.64 (±0.07)	2.7 (±0.3)	0.43 (±0.14)	0.38 (±0.12)	0.16 (±0.05)	0.15 (±0.05)
SUM-10	0.33 (±0.19)	0.72 (±0.04)	0.54 (±0.32)	0.20 (±0.02)	1.9 (±1.1)	1.10 (±0.67)	0.24 (±0.15)	0.48 (±0.30)	0.11 (±0.07)
SUM-2	2.2 (±0.2)	4.9 (±0.4)	0.94 (±0.10)	0.12 (±0.01)	2.5 (±0.2)	0.52 (±0.13)	0.17 (±0.05)	0.15 (±0.04)	0.06 (±0.02)
SUM-0.7	5.3 (±0.4)	12 (±1)	1.03 (±0.10)	0.24 (±0.03)	2.3 (±0.2)	0.86 (±0.24)	0.18 (±0.05)	0.13 (±0.04)	0.04 (±0.01)
SUM-0.4	7.7 (±0.6)	17 (±1)	0.91 (±0.09)	0.24 (±0.01)	1.8 (±0.1)	0.96 (±0.27)	0.25 (±0.07)	0.09 (±0.02)	0.04 (±0.01)
SUM-0.3	8.5 (±2.7)	19 (±6)	0.79 (±0.25)	0.20 (±0.02)	1.5 (±0.5)	1.02 (±0.45)	0.28 (±0.12)	0.08 (±0.03)	0.03 (±0.01)
PME-NR	2.9 (±0.2)	6.4 (±0.5)	0.62 (±0.06)	0.25 (±0.02)	2.9 (±0.2)	0.90 (±0.47)	0.48 (±0.27)	0.18 (±0.10)	0.10 (±0.05)
PME-R	2.7 (±0.4)	6.0 (±0.9)	0.59 (±0.09)	0.28 (±0.05)	2.6 (±0.4)	1.22 (±0.32)	0.75 (±0.22)	0.25 (±0.07)	0.15 (±0.04)
Averages									
WIN					2.9 (±0.3)	0.55 (±0.20)	0.22 (±0.05)	0.16 (±0.06)	0.10 (±0.04)
SUM					2.0 (±0.4)	0.89 (±0.23)	0.30 (±0.06)	0.18 (±0.17)	0.06 (±0.03)
Field blanks^j									
FB1^k	0.016 (±0.001)		0.81 (±0.15)	8.3 (±4.8)					
FB2	0.021 (±0.001)		0.66 (±0.33)	0.54 (±0.07)					
FB3	0.028 (±0.001)		0.97 (±0.17)	0.73 (±0.09)					

[a] Davis winter solstice sunlight-normalized steady-state concentration of $^1O_2^*$.

[b] Production rate of $^1O_2^*$, calculated as $P_{1O2*} = [^1O_2^*] \times k'_{H2O}$, where k'_{H2O} is the first-order rate constant for loss of $^1O_2^*$ in H_2O (2.2×10^5 s^{-1}) (Bilski et al., 1997).

[c] Fraction of probe FFA lost due to $^1O_2^*$ in PME diluted with H_2O, calculated as $f_{FFA,1O2*} = ([^1O_2^*]/2 \times k_{FFA+1O2*})/k'_{FFA,H2O}$, where $k_{FFA+1O2*}$ is the second-order rate constant of FFA reacting with $^1O_2^*$ and $k'_{FFA,H2O}$ is the normalized first-order decay rate of FFA in the PME diluted with H_2O.

[d] Fraction of probe FFA lost due to $^\bullet OH$ in PME diluted with H_2O, calculated as $f_{FFA,OH} = ([^\bullet OH] \times k_{FFA+OH})/k'_{FFA,H2O}$, where k_{FFA+OH} is the second-order rate constant of FFA reacting with $^\bullet OH$ (1.5×10^{10} M^{-1} s^{-1}) (Ross and Ross, 1977), assuming the $^\bullet OH$ concentration is the same in the diluted and undiluted portions of PME.

[e] Apparent quantum yield of $^1O_2^*$, calculated as $\Phi_{1O2*} = P_{1O2*}/R_{abs}$.

[f] Fraction of oxidizing triplets (determined by SYR) in the total triplet pool (Kaur and Anastasio, 2018). f_Δ is the yield of singlet oxygen from the quenching of triplet states by dissolved oxygen, which we assume is 0.53 (McNeill and Canonica, 2016).

[g] Fraction of oxidizing triplets determined by PTA to the total triplet pool.

[h] Ratio of triplet concentration determined by SYR to the singlet oxygen concentration.

[i] Ratio of triplet concentration determined by PTA to the singlet oxygen concentration.

[j] Field blank results were not subtracted from sample results.

[k] This field blank sample was contaminated by a pH electrode and other unknown sources.

S17

Table S9. Parameters in hyperbolic fitting between photooxidant concentration and DOC using Eqn. 11

	WIN		SUM	
	a	*b* (M^{-1})	*a*	*b* (M^{-1})
$^1O_2^*$	2.8 ($\pm$ 0.1) $\times 10^{-10}$[a]	6[a]	4.4 ($\pm$ 0.3) $\times 10^{-10}$	27 ($\pm$ 4)
$^3C^*_{SYR}$	0.85 ($\pm$ 0.46) $\times 10^{-10}$	97 ($\pm$ 86)	1.2 ($\pm$ 0.4) $\times 10^{-10}$	149 ($\pm$ 65)
$^3C^*_{PTA}$	0.44 ($\pm$ 0.05) $\times 10^{-10}$	73 ($\pm$ 15)	0.31 ($\pm$ 0.03) $\times 10^{-10}$	84 ($\pm$ 13)

[a] Since winter samples show no curvature for [$^1O_2^*$] with DOC, to fit data with equation 11, *a* was obtained as the slope of linear regression between [$^1O_2^*$] and DOC, while *b* was obtained by using a fitted line that passed through only the first 4 data points (Figure S5).

Table S10. Second-order rate constants of triplet quenching and reaction with dissolved organic carbon[a]

	$k_{rxn+Q,3C^*}$ (L (mol C)$^{-1}$ s^{-1})		$^3C^*$ probe used
	WIN	SUM	
This work	0.47×10^7[b]	2.1 ($\pm$ 0.3) $\times 10^7$	FFA
	7.6 ($\pm$ 6.8) $\times 10^7$	12 ($\pm$ 5) $\times 10^7$	SYR
	5.7 ($\pm$ 1.2) $\times 10^7$	6.6 ($\pm$ 1.0) $\times 10^7$	PTA
Kaur et al. (2019)[c]	9.3 ($\pm$1.3) $\times 10^7$		SYR
Wenk et al. (2013)[d]	(1.3 – 3.9) $\times 10^7$		-

[a] Rate constants are for DOM quenching and reaction with the pool of triplets that are seen by a given probe. FFA, by reacting with $^1O_2^*$, is likely seeing the DOM reactivity of the entire triplet pool (i.e., both oxidizing and non-oxidizing triplets), SYR is probing the reactivity of both strongly and weakly oxidizing triplets, while PTA is probing only the strongly oxidizing triplets.

[b] This value was calculated using the *b* value (Table S9) that was estimated by fitting the line of equation 11 between [$^1O_2^*$] and DOC through only the first 4 data points (Figure S5).

[c] Value is uncertain because triplet concentrations were not corrected for inhibition of SYR loss caused by DOM.

[d] Rate constant measured for quenching of triplets of 2-acetonaphthone and 3-methoxyacetophenone by surface water dissolved organic matter as determined using laser flash photolysis.

Section S2. Kinetic model for singlet oxygen

We first consider a modified equation for the steady-state $^1O_2^*$ concentration from McNeill et al. (2016) by adding DOC as an additional sink for $^1O_2^*$:

$$[^1O_2^*] = \frac{k_{O2+3C*}[^3C^*][O_2]f_\Delta}{k'_{H2O} + k_{rxn+Q,1O2*}[DOC]} \qquad (S5)$$

where k_{O2+3C*} is the bimolecular rate constant of O_2 quenching $^3C^*$, $[^3C^*]$ is the concentration of triplets that can transfer energy to O_2 (i.e., essentially all triplets), $[O_2]$ is the dissolved oxygen concentration, f_Δ is the fraction of oxygen quenching triplets that produces $^1O_2^*$, k'_{H2O} is the first-order rate constant for loss of $^1O_2^*$ by H_2O (2.2×10^5 s^{-1}) (Bilski et al., 1997), and $k_{rxn+Q,1O2*}$ is the bimolecular rate constant of DOC reacting and quenching $^1O_2^*$.

While DOC will be an important sink for $^1O_2^*$ under ALW conditions (Kaur et al., 2019), in our PM extracts it appears the curvature of $[^1O_2^*]$ with increasing DOC observed in SUM (Fig. 2) is only due to $^3C^*$ since triplets are more sensitive to the presence of organics than is $^1O_2^*$. Therefore, H_2O is the dominant sink, and the quenching of $^1O_2^*$ by DOC is negligible (i.e., $k_{rxn+Q,1O2*}[DOC] << k'_{H2O}$). From Kaur et al. (2019), $^3C^*$ in PME can be expressed as

$$[^3C^*] = \frac{\left(\frac{j_{abs}\Phi_{ISC}f}{k_{O2+3C*}[O_2]}\right)[DOC]}{1 + \left(\frac{k_{rxn+Q,3C*}}{k_{O2+3C*}[O_2]}\right)[DOC]} \qquad (S6)$$

where j_{abs} is the rate constant for light absorption, Φ_{ISC} is the quantum yield of intersystem crossing, f is the fraction of DOC that is in chromophores, and $k_{rxn+Q,3C*}$ is the bimolecular rate constant of DOC reacting with and quenching $^3C^*$.

Substituting this equation for $[^3C^*]$ into equation S5 (after applying $k_{rxn+Q,1O2*}[DOC] << k'_{H2O}$) yields

$$[^1O_2^*] = \frac{\frac{\left(\frac{j_{abs}\Phi_{ISC}f}{k_{O2+3C*}[O_2]}\right)[DOC]}{1 + \left(\frac{k_{rxn+Q,3C}}{k_{O2+3C*}[O_2]}\right)[DOC]} \times k_{O2+3C*}[O_2]f_\Delta}{k'_{H2O}} = \frac{\frac{j_{abs}\Phi_{ISC}f \times f_\Delta}{k'_{H2O}}[DOC]}{1 + \left(\frac{k_{rxn+Q,3C}}{k_{O2+3C*}[O_2]}\right)[DOC]} \qquad (S7)$$

This equation is of the form

$$[^1O_2^*] = \frac{a[DOC]}{1 + b[DOC]} \qquad (S8)$$

where

$$a = \frac{j_{abs}\Phi_{ISC}f \times f_\Delta}{k'_{H2O}} \qquad (S9)$$

$$b = \frac{k_{rxn+Q,3C*}}{k_{O2+3C*}[O_2]} \qquad (S10)$$

Since $[^1O_2^*] = P_{1O2*} / k'_{H2O}$ when DOC is a negligible sink of $^1O_2^*$ (i.e. H_2O is the only sink), the production rate of singlet oxygen can be calculated by

$$P_{1O2*} = \frac{a[DOC]}{1 + b[DOC]} \times k'_{H2O} \qquad (S11)$$

Thus, in our relatively dilute extracts we calculate P_{1O2*} as $[^1O_2^*] \times k'_{H2O}$ (Eq.10), while for extrapolating to ALW conditions we use Eq. S11 to calculate the $^1O_2^*$ production rate.

Table S11. Parameters used for photooxidant concentration extrapolation

Parameters		WIN	SUM
Average DOC/(PM/H$_2$O)[a] (mol C L^{-1})/(µg PM/µg H$_2$O)		16.5	30.7
•OH	$\Delta P_{OH,aq}/\Delta$DOC (M s^{-1}/(mol C L^{-1})[b]	1.6×10^{-6}	-
	$\Delta k'_{OH}/\Delta$DOC (M s^{-1}/(mol C L^{-1})[b]	2.9×10^{8}	2.5×10^{8}
$^1O_2^*$	a[c]	2.8×10^{-10}	4.4×10^{-10}
	b (M^{-1})[c]	6	27
	$k_{DOC+1O2*}$ (L (mol C)$^{-1}$ s^{-1})[d]		1.0×10^5	
$^3C^*_{SYR}$	$\Delta P_{3C*}/\Delta$DOC (M s^{-1}/(mol C L^{-1})[b]	6.2×10^{-5}	9.2×10^{-5}
	$k_{rxn+Q,3C*}$ (L (mol C)$^{-1}$ s^{-1})[e]	7.6×10^{7}	12×10^{8}
$^3C^*_{PTA}$	$\Delta P_{3C*}/\Delta$DOC (M s^{-1}/(mol C L^{-1})[b]	3.4×10^{-5}	2.4×10^{-5}
	$k_{rxn+Q,3C*}$ (L (mol C)$^{-1}$ s^{-1})[e]	5.7×10^{7a}	6.6×10^{7}

[a] Average ratio of DOC to particle mass/water mass ratio for each sample.
[b] Slope of linear regression between production rates or sinks for photooxidant and DOC.
[c] Parameters in regression fit between $[^1O_2^*]$ and DOC using Eqn. 11 in the main text. Production rates of $^1O_2^*$ were calculated using these parameters in Eqn. S11.
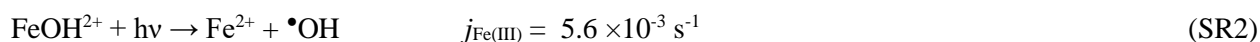[d] Second-order rate constant for loss of $^1O_2^*$ by DOC. The value is estimated using the same approach from Kaur et al. (2019) but is lower than their value of 8.2×10^5 (L (mol C)$^{-1}$ s^{-1}.
[e] Second-order rate constant for reaction and quenching of oxidizing triplets (as determined by SYR or PTA) by DOC.

Section S3. Modeling the $^\bullet$OH production rate in SUM by photo-Fenton reactions

To simulate bimolecular $^\bullet$OH production as a function of particle mass/water mass ratio in SUM, we
assume that photo-Fenton reactions are the dominant sources for $^\bullet$OH. We modeled this using two
reactions (SR1 and SR2) and tuned the reactant concentrations so that calculated $^\bullet$OH production rates
match measured values.

We simplified the suite of photo-Fenton reactions that produce $^\bullet$OH from hydrogen peroxide (H_2O_2)
using two reactions (Benkelberg and Warneck, 1995; Christensen et al., 1993; Mao et al., 2013):

$$Fe^{2+} + H_2O_2 \rightarrow Fe^{3+} + {}^\bullet OH + OH^- \qquad k_1 = 70 \text{ M}^{-1}\text{ s}^{-1} \tag{SR1}$$

$$FeOH^{2+} + h\nu \rightarrow Fe^{2+} + {}^\bullet OH \qquad j_{Fe(III)} = 5.6 \times 10^{-3}\text{ s}^{-1} \tag{SR2}$$

We assume that Fe^{2+} and $FeOH^{2+}$ are the dominant Fe(II) and Fe(III) hydroxide species, respectively,
which is reasonable at pH 4.2 or lower (Faust and Hoigné, 1990; Morgan and Lahav, 2007).
Fe(III)−carboxylate complexes can also undergo photolysis to produce $^\bullet$OH (Southworth and Voelker,
2003; Weller et al., 2014), but we neglect them here. The $^\bullet$OH production rate from SR1 and SR2 is

$$P_{OH} = k_1[Fe^{2+}][H_2O_2] + j_{Fe(III)}[FeOH^{2+}] \tag{S12}$$

Next, we estimate the total dissolved iron and H_2O_2 concentrations so that our calculated P_{OH}
approximately matches the measured values in SUM. To do this, we assume that: (1) The ratio of
[Fe(II)]/([Fe(II)]+Fe(III)]) is a constant 0.85 during daytime (i.e. during our illumination), (Deguillaume
et al., 2005; Weller et al., 2014); (2) H_2O_2 reaches a steady-state concentration during the illumination; (3)
The concentrations of dissolved iron and H_2O_2 increase proportionally with concentration factor (PM
mass/water mass ratio) in our extracts. By setting dissolved iron and H_2O_2 concentrations to 0.4 µM and 3
µM in SUM-10, respectively, the simulated P_{OH} and [$^\bullet$OH] fit well with the measured values across all
dilutions (Figure S4). Meanwhile, the estimated concentrations in SUM-10 are in a reasonable range for
dilute cloud/fog water (Anastasio et al., 1994; Deguillaume et al., 2005; Faust et al., 1993). We next
extrapolate this simple model to ambient PM conditions with one modification: since the aqueous H_2O_2
concentration cannot increase with the particle mass/water mass ratio without limitation (because $H_2O_{2(aq)}$
can partition into the gas phase), we set an upper limit for $H_2O_{2(aq)}$ of 100 µM, which corresponds to a
typical gas-phase H_2O_2 mixing ratio of 1 ppb (Tilgner et al., 2021; Vione et al., 2003) assuming Henry's
law equilibrium ($K_H = 10^5$ M atm^{-1}) (Seinfeld and Pandis, 2008). We assume that the H_2O_2(aq)
concentration increases proportionally with PM mass/water mass ratio until it reaches 100 µM and then is
constant at this value under more concentrated conditions. Our estimated soluble iron concentration of 0.4
µM in SUM-10 predicts a dissolved Fe concentration under ALW conditions (1 µg PM/µg H_2O) of 9.6

mM; we assume this is all dissolved, with no precipitation. This soluble iron concentration is similar to expected dissolved iron concentrations in aqueous aerosols (Gen et al., 2020; Tilgner et al., 2021).
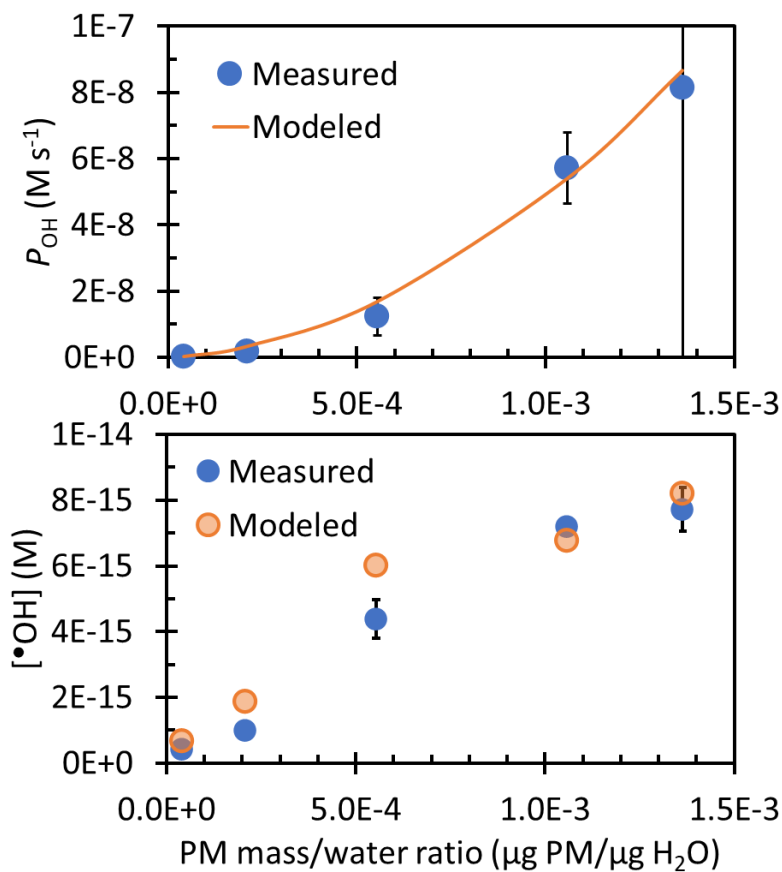
Figure S4. Comparison of measured (blue) and modeled (orange) $^{\bullet}$OH production rates (top panel) and concentrations (bottom panel) in SUM as a function of particle mass/water mass ratio. The modeled $^{\bullet}$OH concentration is calculated using the modeled production rate divided by the measured $^{\bullet}$OH sink (k'_{OH}) at each dilution.
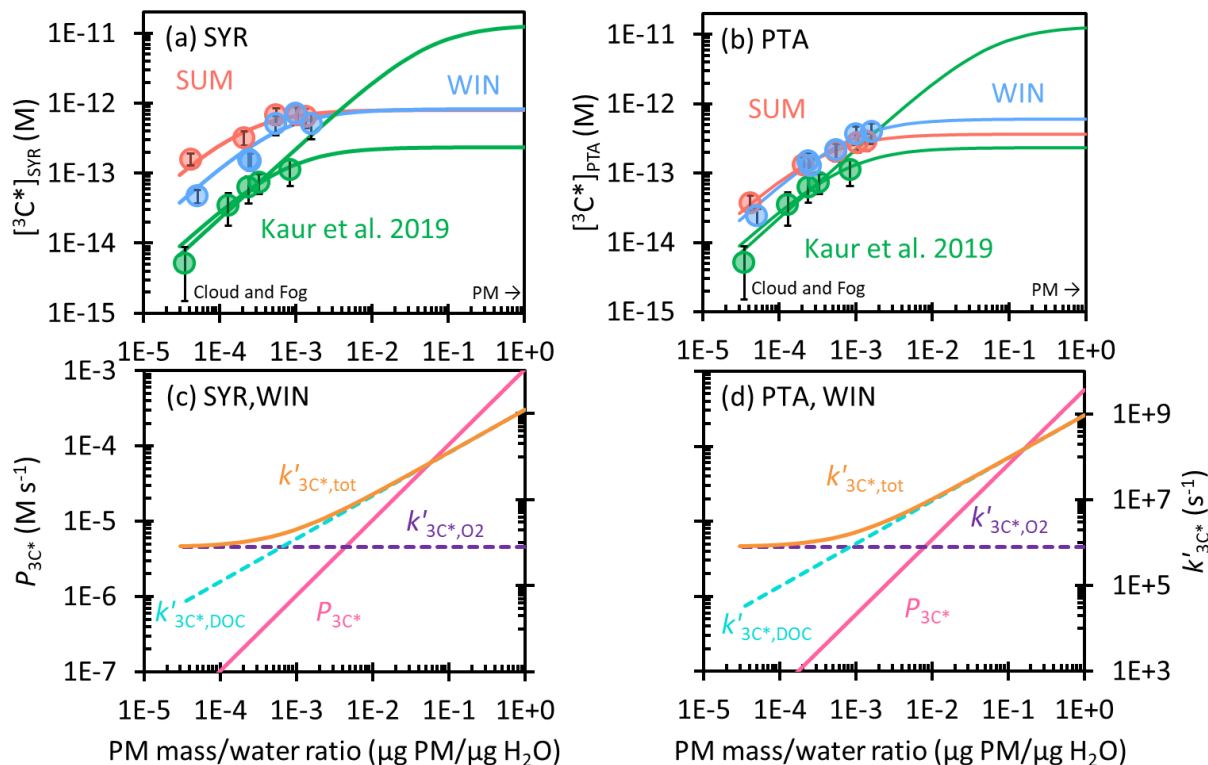
Figure S5. Top row: Triplet excited state concentrations determined by (a) SYR and (b) PTA as a function of particle mass/water mass ratio in WIN extracts (blue) and SUM (red). Solid circles are measured values in dilution experiments, while lines are extrapolations to ALW conditions. Previous measurements and extrapolations (best fit and high estimate) for Davis winter particle extracts are in green (Kaur et al., 2019). Bottom row: Dependence of triplet production rate (red line), and rate constants for $^3C^*$ loss, including quenching by oxygen ($k'_{3C^*,O2}$, purple dashed line), dissolved organic carbon ($k'_{3C^*,DOC}$, blue dashed line), and total sinks ($k'_{3C^*,tot} = k'_{3C^*,O2} + k'_{3C^*,DOC}$, orange solid line), on particle mass/water mass ratio for the WIN sample. Panels (c) and (d) show data determined using SYR and PTA, respectively.
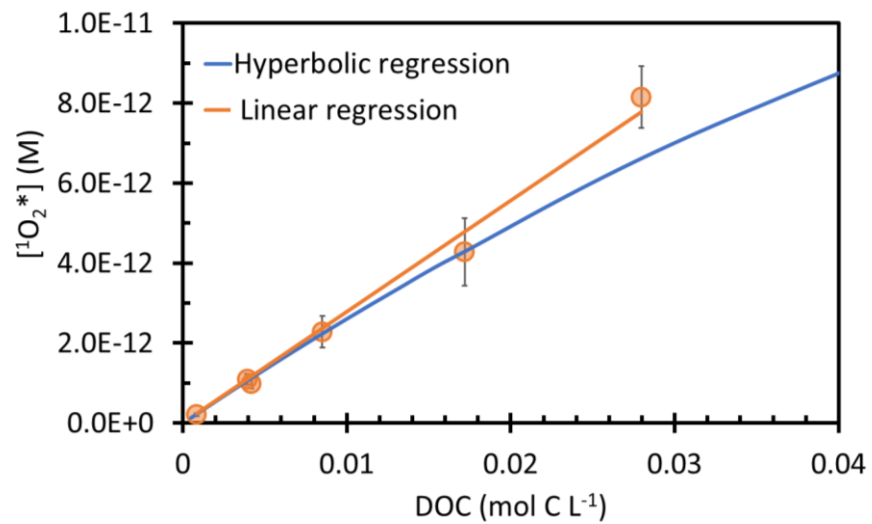
Figure S6. $^1O_2^*$ concentration as a function of DOC in winter samples (circles). The orange line represents a linear regression fit to all points, while the blue line represents a hyperbolic regression fit to the first 4 data points using equation 11 in the main text.
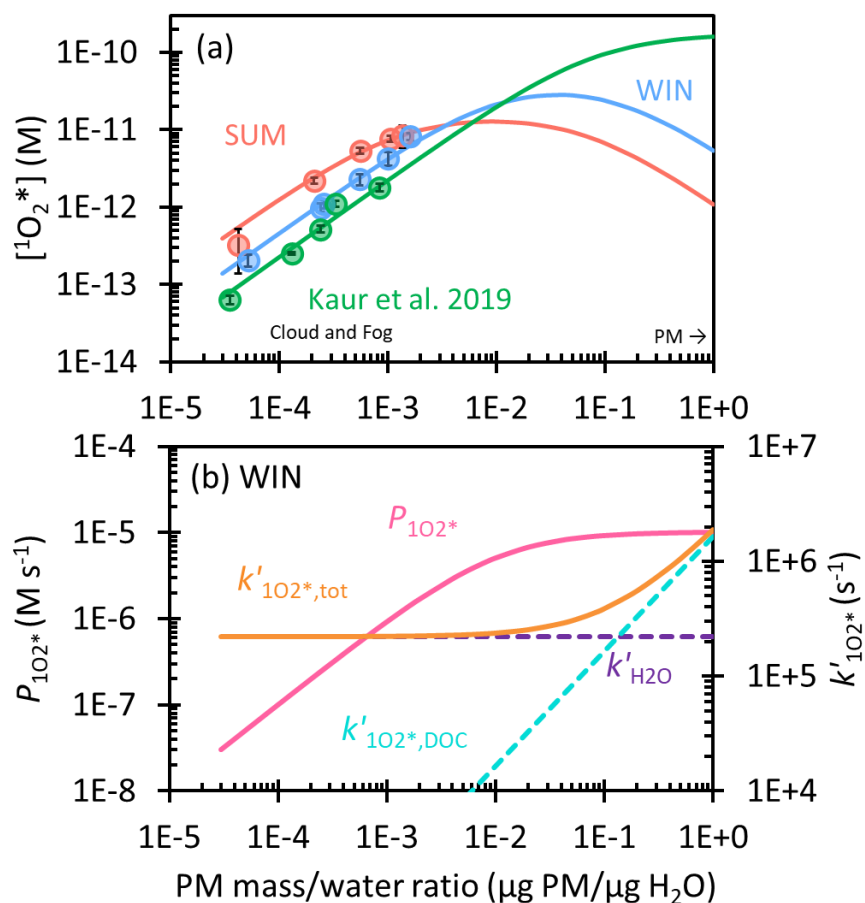
Figure S7. (a) Dependence of singlet molecular oxygen concentration on particle mass/water mass ratio in winter extracts (blue) and summer (red) samples. Solid circles are measured values in dilution experiments, while lines are extrapolations to ALW conditions. Previous measurements and extrapolation with Davis winter particle extracts are in green (Kaur et al., 2019). (b) Singlet oxygen production rate, (P_{1O2*}, red line) and rate constants for $^1O_2*$ loss, including deactivation by water (k'_{H2O}, purple), quenching by dissolved organic carbon ($k'_{1O2*,DOC}$, blue), and total sinks ($k'_{1O2*,tot} = k'_{,H2O} + k'_{1O2*,DOC}$, orange), as a function of particle mass/water mass ratio for winter samples.
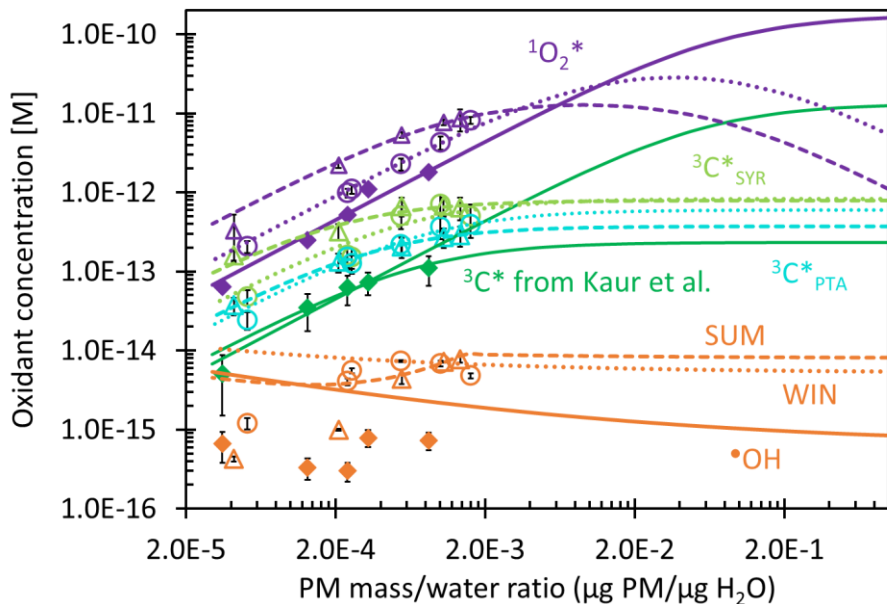
Figure S8. Dependence of photooxidant concentrations on particle mass/water mass ratio in WIN, SUM, and previous Davis winter particle extracts from Kaur et al. (2019). Symbols represent measured values under lab dilution conditions for WIN (open circles), SUM (open triangles), and Kaur et al. (filled diamonds), respectively. Lines represent extrapolations of experimental data to aerosol liquid water conditions for WIN (dotted lines), SUM (dashed lines), and Kaur et al. (solid lines) samples. Singlet oxygen concentrations are in purple; triplet concentrations are in light green for SYR-determined values, blue for PTA-determined values, and dark green for data from Kaur et al.; hydroxyl radical concentrations are in orange. The lines for $^{\bullet}OH$ are generally higher than the experimental measurements because the extrapolations include mass transfer of gas-phase hydroxyl radical to the drop/particle. The gas phase does not appear to be a significant source or sink of particle-phase $^{3}C^{*}$ or $^{1}O_{2}^{*}$.

References

330   Anastasio, C., Faust, B. C. and Allen, J. M.: Aqueous phase photochemical formation of hydrogen peroxide in authentic cloud waters, J. Geophys. Res., 99(D4), 8231, doi:10.1029/94JD00085, 1994.

Anastasio, C. and McGregor, K. G.: Chemistry of fog waters in California's Central Valley: 1. In situ photoformation of hydroxyl radical and singlet molecular oxygen, Atmos. Environ., 35(6), 1079–1089, doi:10.1016/S1352-2310(00)00281-8, 2001.

335   Benkelberg, H.-J. and Warneck, P.: Photodecomposition of Iron(III) Hydroxo and Sulfato Complexes in Aqueous Solution: Wavelength Dependence of OH and SO4- Quantum Yields, J. Phys. Chem., 99(14), 5214–5221, doi:10.1021/j100014a049, 1995.

Bilski, P., Holt, R. N. and Chignell, C. F.: Properties of singlet molecular oxygen in binary solvent mixtures of different polarity and proticity, J. Photochem. Photobiol. A, 109(3), 243–249,
340   doi:10.1016/S1010-6030(97)00147-0, 1997.

Canonica, S. and Laubscher, H.-U.: Inhibitory effect of dissolved organic matter on triplet-induced oxidation of aquatic contaminants, Photochem. Photobiol. Sci., 7(5), 547, doi:10.1039/b719982a, 2008.

Christensen, H., Sehested, K. and Løgager, T.: The reaction of hydrogen peroxide with Fe(II) ions at elevated temperatures, Radiation Physics and Chemistry, 41(3), 575–578, doi:10.1016/0969-
345   806X(93)90022-M, 1993.

Deguillaume, L., Leriche, M., Desboeufs, K., Mailhot, G., George, C. and Chaumerliac, N.: Transition metals in atmospheric liquid phases: sources, reactivity, and sensitive parameters., Chem. Rev., 105(9), 3388–3431, doi:10.1021/cr040649c, 2005.

Faust, B. C., Anastasio, C., Allen, J. M. and Arakaki, T.: Aqueous-phase photochemical formation of
350   peroxides in authentic cloud and fog waters., Science, 260(5104), 73–75, doi:10.1126/science.8465202, 1993.

Faust, B. C. and Hoigné, J.: Photolysis of Fe (III)-hydroxy complexes as sources of OH radicals in clouds, fog and rain, Atmospheric Environment. Part A. General Topics, 24(1), 79–89, doi:10.1016/0960-1686(90)90443-Q, 1990.

355   Gen, M., Zhang, R., Li, Y. and Chan, C. K.: Multiphase photochemistry of iron-chloride containing particles as a source of aqueous chlorine radicals and its effect on sulfate production, Environ. Sci. Technol., 54(16), 9862–9871, doi:10.1021/acs.est.0c01540, 2020.

Kaur, R. and Anastasio, C.: First measurements of organic triplet excited states in atmospheric waters., Environ. Sci. Technol., 52(9), 5218–5226, doi:10.1021/acs.est.7b06699, 2018.

360   Kaur, R., Labins, J. R., Helbock, S. S., Jiang, W., Bein, K. J., Zhang, Q. and Anastasio, C.: Photooxidants from brown carbon and other chromophores in illuminated particle extracts, Atmos. Chem. Phys., 19(9), 6579–6594, doi:10.5194/acp-19-6579-2019, 2019.

Ma, L., Worland, R., Tran, T. and Anastasio, C.: An evaluation of probes to measure oxidizing triplet excited states in aerosol liquid water, Environ. Sci. Technol., In press, 2023.

365   Mao, J., Fan, S., Jacob, D. J. and Travis, K. R.: Radical loss in the atmosphere from Cu-Fe redox coupling in aerosols, Atmos. Chem. Phys., 13(2), 509–519, doi:10.5194/acp-13-509-2013, 2013.

McNeill, K. and Canonica, S.: Triplet state dissolved organic matter in aquatic photochemistry: reaction mechanisms, substrate scope, and photophysical properties., Environ. Sci. Process. Impacts, 18(11), 1381–1399, doi:10.1039/c6em00408c, 2016.

370   Morgan, B. and Lahav, O.: The effect of pH on the kinetics of spontaneous Fe(II) oxidation by O2 in aqueous solution--basic principles and a simple heuristic description., Chemosphere, 68(11), 2080–2084, doi:10.1016/j.chemosphere.2007.02.015, 2007.

Ross, F. and Ross, A. B.: Selected specific rates of reactions of transients from water in aqueous solution. III. Hydroxyl radical and perhydroxyl radical and their radical ions, Historical Energy Database (United
375   States)., 1977.

Seinfeld, J. and Pandis, S.: Atmospheric chemistry and physics: from air pollution to climate change. John Wiley & Sons, 2016.

Smith, J. D., Kinney, H. and Anastasio, C.: Aqueous benzene-diols react with an organic triplet excited state and hydroxyl radical to form secondary organic aerosol., Phys. Chem. Chem. Phys., 17(15), 10227–
380   10237, doi:10.1039/c4cp06095d, 2015.

Smith, J. D., Kinney, H. and Anastasio, C.: Phenolic carbonyls undergo rapid aqueous photodegradation to form low-volatility, light-absorbing products, Atmos. Environ., 126, 36–44, doi:10.1016/j.atmosenv.2015.11.035, 2016.

Southworth, B. A. and Voelker, B. M.: Hydroxyl radical production via the photo-Fenton reaction in the
385   presence of fulvic acid., Environ. Sci. Technol., 37(6), 1130–1136, doi:10.1021/es020757l, 2003.

Tilgner, A., Schaefer, T., Alexander, B., Barth, M., Collett Jr., J. L., Fahey, K. M., Nenes, A., Pye, H. O. T., Herrmann, H. and McNeill, V. F.: Acidity and the multiphase chemistry of atmospheric aqueous particles and clouds, Atmos. Chem. Phys., 21(17), 13483–13536, doi:10.5194/acp-21-13483-2021, 2021.

Tratnyek, P. G. and Hoigne, J.: Oxidation of substituted phenols in the environment: a QSAR analysis of
390   rate constants for reaction with singlet oxygen, Environ. Sci. Technol., 25(9), 1596–1604, 1991.

Vione, D., Maurino, V., Minero, C. and Pelizzetti, E.: The atmospheric chemistry of hydrogen peroxide: a review., Ann. Chim., 93(4), 477–488, 2003.

Weller, C., Tilgner, A., Bräuer, P. and Herrmann, H.: Modeling the impact of iron-carboxylate photochemistry on radical budget and carboxylate degradation in cloud droplets and particles., Environ.
395   Sci. Technol., 48(10), 5652–5659, doi:10.1021/es4056643, 2014.

Wenk, J., Eustis, S. N., McNeill, K. and Canonica, S.: Quenching of excited triplet states by dissolved natural organic matter., Environ. Sci. Technol., 47(22), 12802–12810, doi:10.1021/es402668h, 2013.

Wenk, J., von Gunten, U. and Canonica, S.: Effect of dissolved organic matter on the transformation of contaminants induced by excited triplet states and the hydroxyl radical., Environ. Sci. Technol., 45(4),
400   1334–1340, doi:10.1021/es102212t, 2011.